

**Human Movement Sciences
Sport, Exercise & Health (research)**

Research Internship Research Master 2014-2015

**Resting-state activity in Parkinson's
disease: bimodal frequency
distribution in phase oscillators on
complex networks**



VU University Amsterdam
Faculty of Human Movement Sciences
Qualification: MSc in Human Movement Sciences
Research internship Research Master

Author: *S.D. Kulik*

Supervisors: *prof. dr. A. Daffertshofer*

Abstract

Parkinson's disease (PD), is a neurodegenerative disorder characterized by a dopamine degeneration leading to primarily motor symptoms, such as akinesia, bradykinesia, rigidity and tremor. In PD, neural oscillations change in the cortex. As shown by previous studies, there is an increase in alpha power, a decrease in beta power and a general slowing of oscillations in the course of the disease. Because the aforementioned studies are descriptive, the cause of oscillatory changes and the impact to neural functioning are not known yet. Therefore, models to describe the qualitative effects of these changes are needed to provide insight in whether slowing of oscillations influence the increase in alpha power and the decrease in beta power, or whether there is another causality. In this study, the aim is to gain more insight into oscillatory changes, whereby a model describing frequencies by means of a preferential rewiring method with a sparse non-growing network of coupled phase oscillators is used as a starting point. A limitation to this model is the unimodal frequency distribution, and therefore, a bimodal frequency distribution will be implemented. The main question is: *Does the description of resting-state MEG data in Parkinson's disease require bimodality in the frequency distribution of its generating oscillator network?* The simultaneous oscillatory changes in alpha and beta band in PD suggest a dependency of these frequencies. Therefore, a model including multiple frequencies is included to understand changes in cortical activities in this disease. A bimodal frequency distribution of the generating oscillator network is successfully applied to numerically simulated data of order parameters' dynamics, which provides a proof of concept for the proposed method. By applying the same approach to resting-state MEG time-series of PD patients, it can be concluded that the bimodal frequency distribution does not capture the simultaneous changes in oscillatory activity as is seen in PD.

Key words

Brain oscillations; Neural synchronization; Kuramoto model; Bimodal distribution; Parkinson's disease

Table of Contents

1 Introduction 3

1.1 Neural oscillations 3

1.2 Neural synchronization 3

1.3 Parkinson’s disease 4

1.4 Brain imaging techniques 4

1.5 The Kuramoto model 5

1.6 Stochastic dynamics 5

1.7 Previous research 6

1.8 Thesis outline..... 6

2 Methods & Procedures 7

2.1 Numerical analysis..... 8

2.1.1 Order parameters’ dynamics 8

2.1.2 Analytics of the oscillators dynamics..... 13

2.2 Empirical data 14

3 Results 16

3.1 Numerical analysis..... 16

3.1.1 Order parameters’ dynamics 16

3.1.2 Oscillators’ dynamics 22

3.2 Empirical data 28

4 Discussion 31

4.1 General conclusions 31

4.2 Previous studies 31

4.3 System identification approach..... 31

4.4 Model comparison..... 32

4.5 Numerical simulations and empirical data 33

5 Conclusions 35

Appendices

Appendix A - Oscillators' dynamics simulated too short..... 36

Appendix B - Comprehensive model comparison results 41

6 References 43

1 Introduction

1.1 Neural oscillations

Neural oscillations represent synchronous activity of single neurons or of many thousands of neurons. In single neurons, oscillatory activity can arise through oscillations in membrane potential or as rhythmic activity of action potentials (ACs). Thereby, voltage-gated channels are only selective for certain ion types and are activated at various potential ranges. This leads to the generation of activities including neural oscillation at multiple frequencies (Buzsáki, 2006). Activity of many thousands of neurons can lead to macroscopic oscillations, which arise from feedback connections between these neurons and can result in synchronization of their firing patterns. This activity is self-sustained and constitutes a robust pattern which is continuously active and generated from within. An input is required to start activity, although it does not prescribe the type of activity that is exhibited. The generation of oscillations is determined by the oscillatory phase and its assimilation. This process can be achieved either by an endogenous energy supply through local interactions between excitatory and inhibitory neurons, or by a random and unclear outside force (Fell & Axmacher, 2011; Sejnowski & Poggio, 2007). Oscillations provide the exchange of information between different brain areas. This interaction is performed best when two communicating assemblies have resonant frequencies, in which the neurons influence each other through excitatory and inhibitory synaptic connections. Hereby, the thalamus is seen as a large communication center where different brain areas are connected. Most connections formed by the thalamus are reciprocal and recurrent which form feedback loops that support oscillatory activity (Buzsáki, 2006; Fell & Axmacher, 2011; Olde Dubbelink et al., 2013; van Wijk, Beek, & Daffertshofer, 2012)

1.2 Neural synchronization

Synchronization of neurons leads to multiple, simultaneous synaptic inputs, resulting in rapid depolarizations which increase the postsynaptic membrane potential to rise above the firing threshold. This process may support neural communication (Fell & Axmacher, 2011).

Oscillators are synchronized when their phase difference equals zero. The difference between phase synchrony and phase asynchrony is displayed in figure 1. As stated by Buzsáki in his book *Rhythms Of The Brain*, the essence of neural synchrony can be defined as: 'coupling through time by some invisible links' (Buzsáki, 2006, p.150). In this definition, 'time' is essential. Synchrony is only achieved when two or many neurons fire within a certain (short) time interval. Only time does not satisfy functional synchronization though. When the physical distance between neurons differ, the AC can be sent at the same time but because it has to cover a longer distance, the moment at which the AC is received can differ and therefore will be seen as asynchronous. It is therefore important for a neuron or neuronal pool to determine a discrete temporal window, composed of milliseconds to seconds, where an earlier input is preserved to be able to alter the response to a subsequent event. Synchronization can be reached when this results in multiple events being integrated over time, leading to the postsynaptic membrane potential to rise above the firing threshold. New ACs that occur outside this time window will have no impact on earlier ACs. Although the ACs have similar meaning, their concurrent occurrence is a coincidence, they are not causally related. A leaky (charged) neuron can integrate over a much shorter time window than when it is at rest (Buzsáki, 2006).

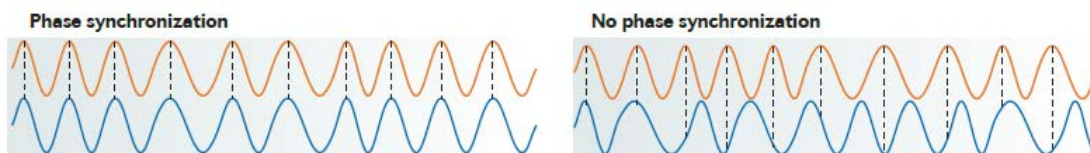


Figure 1: The difference between phase synchrony and asynchrony, visualizing phase assimilation and no phase assimilation respectively. (Figure adapted from Fell & Axmacher (2011)).

For communication between networks of neurons (brain regions), displayed in figure 2, synchronization is essential. Within a network of neurons, the time window for synchronization becomes longer and is determined by the readiness potential, which defines the activity leading up to voluntary muscle movement. Buzsáki and Fell & Axmacher state that there is a correlation between the time window in which spikes can occur and the frequency at which neural areas synchronize. A slower rhythm increases the chance of synchronization because more neurons within a bigger part of the brain can be recruited, and vice versa. Thereby, when there is a slower rhythm, the restrictions of axonal and synaptic delays decrease and the extent in space increases (Buzsáki, 2006; Fell & Axmacher, 2011).

In large-scale oscillations, local and global synchronization refer to the difference between synchrony within a neural ensemble and synchrony between neural ensembles, respectively. Global synchronization is caused by bidirectional coupling between all brain areas which create feedback loops and long-range connections (Buzsáki, 2006; Fell & Axmacher, 2011; Schnitzler & Gross, 2005; Sejnowski & Poggio, 2007). Local information processing is represented by local field potentials (LFPs), and entails fluctuations in membrane potentials of local neuronal populations. The structural basis of local functional networks are short-range connections. These networks control an important aspect of brain functioning in regulating cognitive, behavioural and motor processes. The oscillations of locally synchronized populations can be classified into different frequency bands: delta (1-4 Hz), theta (4-8 Hz), alpha (8-13 Hz), beta (13-30 Hz) and gamma (30-70 Hz). The functional association of these frequency bands, however, may depend on the brain region considered. Alpha/mu, beta and gamma oscillations, for example, show strong movement-related modulations in large parts of the motor system. Successful motor functioning depends on the interactions and timing between multiple brain regions (Berendse & Stam, 2007; Engel & Fries, 2010; Olde Dubbelink, 2014; Schnitzler & Gross, 2005; van Wijk et al., 2012).

As stated by Buzsáki, 'brain "state" is a macroscopic variable, reflected by the mean field behaviour of the system, typically a characteristic oscillatory mode or a transition between different oscillatory modes' (Buzsáki, 2006, p. 175). The resting-state of the brain, which entails the absence of a specific task, exhibits spatiotemporally structured patterns of ongoing activity, known as resting-state networks or resting-state functional connectivity. In these networks, when the neurons do not rise above threshold level, and when coupling is sufficient, all units oscillate leading to irregular dynamics exhibited by the network. The functional connectivity pattern that thereby arises is largely reproducible despite its irregular nature. Abnormalities in this pattern indicate reduced quality of cerebral networks and health status of the brain. It is therefore considered as a biomarker in ageing and different pathologies (Deco, Buehlmann, Masquelier, & Hugues, 2011; Ferreira & Busatto, 2013; Sadaghiani, Hesselmann, Friston, & Kleinschmidt, 2010).

1.3 Parkinson's disease

Changes in neural synchrony is a common symptom in many neurodegenerative diseases, including Parkinson's disease (PD). This leads to changes in (local) oscillatory synchrony, involving multiple frequencies, and changes in functional connectivity between brain areas. PD is characterized by a dopamine degeneration leading to multiple primarily motor symptoms, such as akinesia, bradykinesia, rigidity and tremor. The dopaminergic degeneration in the substantia nigra pars compacta leads to an increase in network connectivity, which will increase the synaptic connections in the basal ganglia for their synapses are suppressed by dopamine. The increase of connections will lead to a more synchronized state of activity which prevents the execution of new movement (akinesia). This increased state of synchronization mostly occurs in the beta band, influencing cortico-cortical functional connectivity (Berendse & Stam, 2007; Rubchinsky, Park, Worth, 2013). Another common deficit in PD is a slowing of resting-state neural oscillations, which is already visible in early-stage PD patients, and entails increased power for low frequency bands and decreased power for higher frequency bands (Berendse & Stam, 2007; Olde Dubbelink et al., 2013). Using spectral analysis of magnetoencephalography (MEG) and electroencephalography (EEG) recordings, Olde Dubbelink et al. showed that slowing of oscillations is a continuous and disease-related process that starts early in PD, is progressive over time and is strongly related to a decline in cognitive function and, to a lesser extent, increasing motor impairments (Olde Dubbelink et al., 2013). Olde Dubbelink et al. also showed increased resting-state functional connectivity in the lower alpha band, which suggests a re-mapping of cortical functional connectivity with disease progression.

1.4 Brain imaging techniques

Changes in both neural oscillations and functional networks in neurological pathologies, for example in PD, can be detected by functional brain imaging techniques such as MEG/EEG. In MEG, magnetic field changes which correspond to voltage changes, i.e. oscillations in the brain, can be detected outside the head. A spatial summation of LFPs is required for the oscillations to be strong enough to allow for recordings. The amplitude of the signal is composed of the degree of synchronization and strength of the LFPs, their spatial orientation and the extent of the involved neuronal population. MEG is especially useful in capturing the

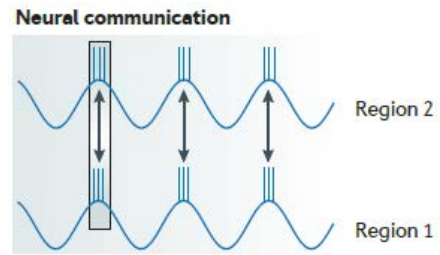


Figure 2: Phase synchronization between brain regions. Figure adapted from Fell & Axmacher (2011)

spatiotemporal dynamics of brain activity, which is applicable to the analysis of structural changes in pathology (Berendse & Stam, 2007; Buzsáki, 2006; Olde Dubbelink et al., 2013; Schnitzler & Gross, 2005).

As described above, brain activity can feature multiple frequencies and evolves over time. Frequency and time cannot be analyzed simultaneously though, because they are mathematically orthogonal. Therefore, they are split up and measured separately by applying different methods. With a Fourier analysis, the signal measured by MEG/EEG is transformed from the time domain into the frequency domain. The signal is thereby represented in sine waves, which include the prevalent frequencies displayed in the power spectrum. The temporal domain is thereby ignored (Buzsáki, 2006).

1.5 The Kuramoto model

A mathematical method to model neural oscillations is the Kuramoto model of coupled phase oscillators. This model is symmetrical and idealized but can exhibit non-trivial collective dynamics. It analyzes synchronization in neural networks, with respect to each phase oscillator in a network:

$$\frac{d\varphi_i(t)}{dt} = \omega_i + \frac{\kappa}{N} \sum_{j=1}^N \sin(\varphi_j(t) - \varphi_i(t)), \quad i = 1, \dots, N \quad (1)$$

With N coupled phase oscillators $\varphi_i(t)$, having natural frequencies ω_i with a given probability density $g(\omega)$ and coupling strength κ which is equal between all pairs of oscillators. $g(\omega)$ is usually symmetric and unimodal, such as a Lorentzian or Gaussian distribution with mean ω_0 . The model specifies global (all-to-all) coupling by means of a sinusoidal interaction function. When the distribution of phase differences is narrow, there is synchronization. With a widely distributed phase difference, coupling in the system is too weak to generate synchronization, i.e. the system is in the desynchronised state. A certain threshold of coupling (κ_c) needs to be exceeded before coherent behaviour of the system occurs, leading to partial or complete synchronization of the phases. This situation refers to a state where the phases are identical or differ by π , which leads to the elimination of the interaction function. Overall, a single attracting synchronous and a single unstable antiphase are captured by the model.

The state of the oscillator at time t can be described by a continuous distribution function $f(\omega, \varphi, t)$, within the limit $N \rightarrow \infty$:

$$\int_0^{2\pi} f(\omega, \varphi, t) d\varphi = g(\omega). \quad (2)$$

and $g(\omega)$ indicating frequency distributions of the oscillator which are not dependent on time (Acebrón, Bonilla, Vicente, Ritort, & Spigler, 2005; Breakspear, Heitmann, & Daffertshofer, 2010; Ott & Antonsen, 2008).

Coherence in the system is measured by the complex order parameter:

$$\rho e^{i\psi} = \frac{1}{N} \sum_j e^{i\varphi_j}, \quad (3)$$

where $0 \leq \rho(t) \leq 1$ measures the coherence of the oscillators (phase uniformity), and $\psi(t)$ is the mean phase. $\rho(t)$ approaches zero when the phases are uniformly distributed, i.e. the system is desynchronised, and approach one when the phases converge, i.e. when all phases are synchronised (Acebrón et al., 2005; Breakspear et al., 2010; Ott & Antonsen, 2008).

1.6 Stochastic dynamics

A stochastic system can be characterized by the presence of uncorrelated random dynamic noise. In a neural network with both excitatory and inhibitory neurons, complex properties such as nonlinearity can be generated. Minor changes in the network can invoke enormous changes in activity. The variability of neuronal responses to every task is approximated as noise and is added internally or externally by or to brain activity. Noise can add up to an input whereby the membrane potential at first was below threshold to as yet cause an AP. This mechanism is referred to as stochastic resonance and provides improved communication between neurons or neuron assemblies (Buzsáki, 2006).

In a stochastic system, random fluctuations typically influence the time evolution of the process. This implies that the future state of this system cannot be determined exactly but can only be estimated. This estimation contains the prediction of conditional probabilities for a future state to occur at a specific point in time and space. A probability distribution function thereby indicates the likelihood of the occurrence of specific states, and is applied in a system identification approach to identify the dynamics of a system (Daffertshofer, 2010).

When a dynamical system undergoes a transition from for example asynchrony to synchrony, this transition corresponds to a bifurcation. These bifurcations qualify the behaviour of the system under vari-

ous circumstances and are therefore informative to analyse the system. There are multiple forms of bifurcations which all belong to a certain type of behaviour exerted by the dynamical system at hand (Buzsáki, 2006; Sejnowski & Poggio, 2007). The Kuramoto model of coupled oscillators is linearly stable when coupling constant $\kappa < \kappa_c$. The system switches from stability to instability from the desynchronized state when $\kappa > \kappa_c$. The synchronized state is non-linearly stable which coincides with a nonlinear stabilization of the synchronized state (Acebrón et al., 2005).

1.7 Previous research

Coopmans used the aforementioned system identification approach to estimate the order parameter dynamics in Kuramoto networks under impact of additive random fluctuations. She also modified the all-to-all coupling by modifying the connectivity matrix between the phase oscillators. For this she used a preferential rewiring method with a sparse non-growing network of coupled Kuramoto phase oscillators to model resting-state PD data. In this study, it was shown that this method proved to be applicable in modelling cortical synchronization (Coopmans, 2013). To further test this method, in the recent study, the same model will be applied to resting-state PD data. Also, another method to model synchronization in resting-state PD data will be applied, focusing on the spectral distribution of the data. In this method a bimodal frequency distribution, as described by Martens et al., will be implemented to increase the accuracy of the Kuramoto model. With a bimodal frequency distribution, changes of multiple frequencies can be captured and modelled. The Kuramoto model will fail here by only coping with a simple polynomial, which will not be sufficient in analysing multiple frequencies. The bimodal model as described by Martens et al., consists of a frequency distribution $g(\omega)$ with two peaks that is the sum of two identical unimodal distributions. With this model, instead of a critical coupling threshold, a multi stable period arises including standing wave states (Martens et al., 2009).

1.8 Thesis outline

As described above, in PD, a change in resting-state oscillations occurs affecting the alpha and beta frequency band. The application of a Kuramoto model with a bimodal frequency distribution for this data might hence be a more comprehensive approach when analysing the dynamics of PD resting-state activity than considering a unimodal frequency distribution as Coopmans did previously.

The main question in the present study is: *Does the description of resting-state MEG data in Parkinson's disease require bimodality in the frequency distribution of its generating oscillator network?* The focus thereby will be on differences in frequencies of brain dynamics between early and late stages of PD. The simultaneous changes in alpha and beta frequency band in Parkinson's disease suggest an interdependency between these frequencies. Here, it is expected that multiple frequencies should be included to understand changes in cortical activities in PD.

The current study consists of three consecutive parts, whereby both numerically simulated and empirical data are analysed. The first part consists of numerical simulations of the order parameters' dynamics in accordance with the article of Martens et al. (2009), to mimic their analysis. A bimodal version of the Kuramoto model, also proposed by Martens et al. (2009), is thereby set up and applied in all three parts of the current study. The second part consists of numerical simulations of the oscillators' dynamics. The third part comprises the analysis of MEG resting-state data of PD patients, obtained from the VU medical centre. Subsequently, in all three parts, a bifurcation analysis will be applied to conduct the stability characteristics of the dynamical systems, and to qualify the synchronization dynamics. To further define the dynamics, the aforementioned system identification approach, based on the estimation of Kramers-Moyal coefficients, as proposed by Daffertshofer (Daffertshofer, 2010) is applied. For this analysis, I hypothesize, as stated by Martens et al., the appearance of standing wave states, as a consequence of the bimodality of frequencies. This bimodality causes the system, when coupling strength is sufficient, to separate into two large groups of synchronized oscillators, representing standing wave states.

According to Martens et al. the synchronization (order parameter) dynamics obey a polynomial form, hence, the simulated data will be fitted accordingly. Whether the proposed polynomials are actually the best fitting models to the data is then determined by the Aikake Information Criterion (AIC) and the Bayesian Information Criterion (BIC).

The overall goal of the current study is to relate the bimodal Kuramoto model to resting-state MEG PD data. Because in PD, multiple frequencies change, it is expected that the bimodal Kuramoto model will give better results in simultaneously analysing these frequencies in PD resting-state data in comparison to the unimodal model as described by Coopmans.

2 Methods & Procedures

Figure 3 displays an overview of the different parts of this study, including the analyses and outcomes of the numerically simulated and empirical data.

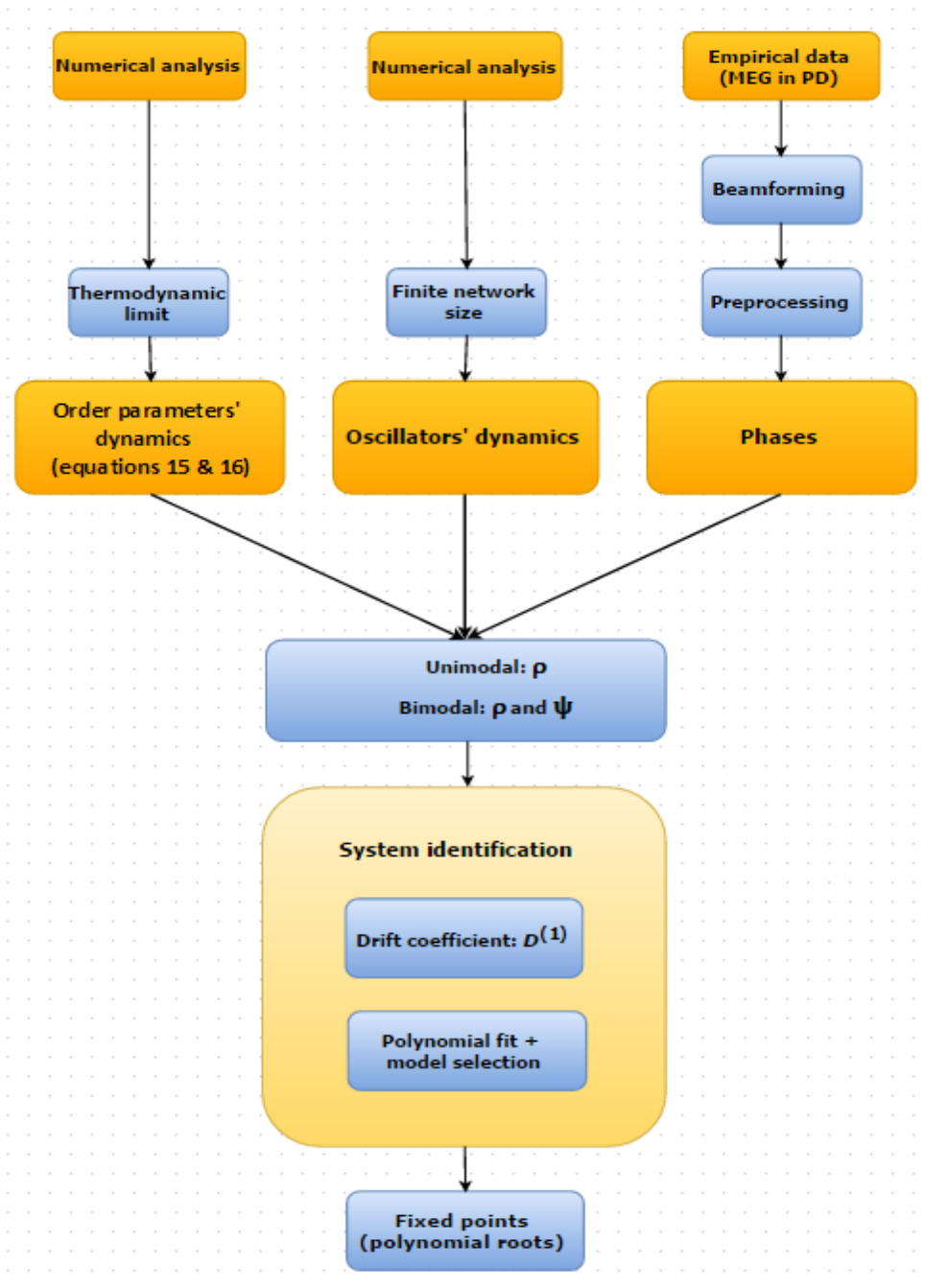


Figure 3: Flowchart comprising an overview over the method as applied to both numerical simulations and empirical data.

2.1 Numerical analysis

2.1.1 Order parameters' dynamics

The Kuramoto model for N phase oscillators can be described as follows:

$$\frac{d\varphi_i(t)}{dt} = \omega_i + \frac{\kappa}{N} \sum_{j=1}^N \sin(\varphi_j(t) - \varphi_i(t)), \quad i = 1, \dots, N \quad (4)$$

Describing N phase oscillators $\varphi_i(t)$, with natural frequencies ω_i and coupling strength κ (Ott & Antonsen, 2008). At a critical value, κ_c , the system will spontaneously start to synchronise, eventually leading to coherent behaviour of the oscillators. In the thermodynamic limit of infinitely many oscillators, i.e. for $N \rightarrow \infty$, the onset of synchronization, occurs at a critical coupling which reads:

$$\kappa_c = \frac{2}{\pi g(0)}. \quad (5)$$

Together with the Lorentzian or Cauchy density: $g(\omega) = \frac{\Delta}{\pi(\Delta^2 + \omega^2)}$, this results in the exact value: $\kappa_c = 2\Delta$ (Strogatz, 2000).

In this study, a bimodal frequency distribution of the natural frequencies given by the sum of two Lorentzians, is applied according to:

$$g(\omega) = \frac{\Delta}{2\pi} \left(\frac{1}{(\omega - \omega_0)^2 + \Delta^2} + \frac{1}{(\omega + \omega_0)^2 + \Delta^2} \right), \quad (6)$$

where Δ represents the width parameter of each Lorentzian and $\pm\omega_0$ are their center frequencies (Martens et al. 2009), as represented in figure 4. $g(\omega)$ is symmetric about zero when the system is unimodal and the system is bimodal when $g(\omega)$ is symmetric around its mean frequency. The bimodality appears when $\omega_0 > \frac{\Delta}{\sqrt{3}}$, which assures sufficient distance between the two peaks. If this distance is not achieved, the distribution is unimodal and resembles the conventional Kuramoto model. For the numerical simulations, the range of ω_0 -values was chosen to cover both a uni- and bimodal distribution (Martens et al., 2009).

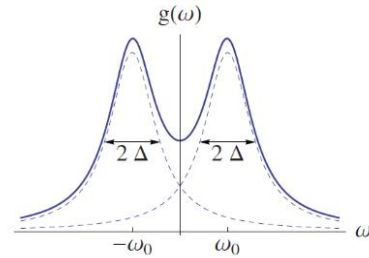


Figure 4: Bimodal frequency distribution (solid blue line) consisting of the sum of two Lorentzian distributions. The dotted line represents two independent Lorentzian distributions (figure adopted from Martens et al., (2009))

To quantify synchronization, the complex order parameter of the dynamical system is defined by:

$$z(t) = \int_{-\infty}^{\infty} \int_0^{2\pi} e^{i\varphi} f(\varphi, \omega, t) d\varphi d\omega. \quad (7)$$

where φ is the phase of an oscillator at time t , and z is the complex order parameter. $|z(t)|$ (equal to ρ) represents the order parameter, referring to phase synchronization, which entails global synchrony in a network (Daffertshofer, 2010). The influence of coupling strength, including critical coupling value κ_c , on the order parameter in the conventional Kuramoto model is displayed in figure 5.

According to Martens et al., the evolution of the two sub-order parameters in a bimodal distribution yield:

$$\dot{z}_1 = -(\Delta_1 + i\omega_{01})z_1 + \frac{\kappa}{4} [z_1 + z_2 - (z_1^* + z_2^*)z_1^2] \quad (8)$$

$$\dot{z}_2 = -(\Delta_2 - i\omega_{02})z_2 + \frac{\kappa}{4} [z_1 + z_2 - (z_1^* + z_2^*)z_2^2] \quad (9)$$

Where, because of the symmetry assumption, $\Delta_1 = \Delta_2$, and $\omega_{01} = \omega_{02}$. To reduce the dimensionality of the system, polar coordinates are introduced ($z_j = \rho_j e^{i\phi_j}$) to define the phase difference: $\psi = \phi_2 - \phi_1$. This results in a three-dimensional system:

$$\dot{\rho}_1 = -\Delta\rho_1 + \frac{\kappa}{4}(1 - \rho_1^2)(\rho_1 + \rho_2 \cos \psi) \quad (10)$$

$$\dot{\rho}_2 = -\Delta\rho_2 + \frac{\kappa}{4}(1 - \rho_2^2)(\rho_1 \cos \psi + \rho_2) \quad (11)$$

$$\dot{\psi} = 2\omega_0 - \frac{\kappa}{4} \frac{\rho_1^2 + \rho_2^2 + 2\rho_1^2\rho_2^2}{\rho_1\rho_2} \sin \psi \quad (12)$$

By subsequently satisfying the symmetry condition $\rho_1(t) = \rho_2(t) \equiv \rho(t)$, the analysis reduces to the phase plane (Martens et al., 2009):

$$\dot{\rho} = \frac{\kappa}{4}\rho \left(1 - \frac{4\Delta}{\kappa} - \rho^2 + (1 - \rho^2) \cos \psi \right) \quad (13)$$

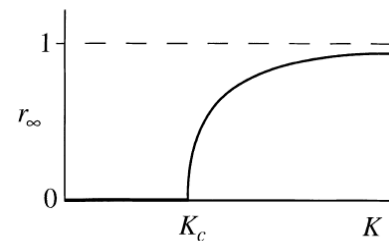


Figure 5: Theoretical behaviour of the order parameter and the influence of coupling strength on synchronization (figure adopted from Strogatz, 2000)

$$\dot{\psi} = 2\omega_0 - \frac{\kappa}{2}(1 + \rho^2) \sin \psi \tag{14}$$

Equation (13) and (14), representing the deterministic dynamics of the system, were applied to simulate time series of the order parameters to illustrate consistency with the paper by Martens et al. (2009). The analysis includes the addition of Gaussian noise to resemble a stochastic dynamical system. That is, the stochastic dynamics were simulated according to:

$$\dot{\rho} = \frac{\kappa}{4}\rho \left(1 - \frac{4\Delta}{\kappa} - \rho^2 + (1 - \rho^2) \cos \psi\right) + \sqrt{2Q_\rho} \Gamma_\rho(t) \tag{15}$$

$$\dot{\psi} = 2\omega_0 - \frac{\kappa}{2}(1 + \rho^2) \sin \psi + \sqrt{2Q_\psi} \Gamma_\psi(t) \tag{16}$$

with $\Gamma_\rho(t)$ and $\Gamma_\psi(t)$ representing uncorrelated Gaussian white noise and Q_ρ and Q_ψ being small parameters. Numerical integration is realized by a simple Euler Maruyama forward algorithm with fixed step size $\Delta t = 5 * 10^{-4}$. To have a wide view on the behaviour of the dynamical system, the simulations of these equations consisted of initial values of ρ within the incremental range $[0, 1]$, with steps of 0.01. For the bimodal model, the initial values of ψ are randomly chosen, for every value of ρ , from the interval $[0, 2\pi]$. This system was then simulated until asymptotic behaviour emerged. The order parameters modulo $(|z(t)|)$ was subsequently calculated for different coupling strengths to produce the bifurcation diagram. Table 1 lists the parameter settings that were applied in the numerical simulations of equation (15) and (16) to reach asymptotic behaviour. A distinction has been made between simulating a 'unimodal' and 'bimodal' version of the Kuramoto model. The bimodal model has thereby been analyzed with $\omega_0 = 1$ and $\omega_0 = 2$, creating two bimodal states to therewith have a wider view on the behaviour of the dynamical system.

Table 1: Parameter settings for the numerical simulations of the order parameters' dynamics (equation (15) and (16))

Parameter	Settings 'unimodal'	Settings 'bimodal'
N	50 000	50 000
T	25	25
ω_0	0	1 and 2
Δ	0.5	0.5
κ	0: 0.05: 5	0: 0.1: 10
Δt	$5 * 10^{-4}$	$5 * 10^{-4}$
Q_ρ	10^{-4}	10^{-4}
Q_ψ	0	0

System identification

Subsequently, a system identification approach is applied to extract the deterministic components from the order parameters' time series, which is based on the calculation of probability densities. The aim thereby is to provide a proof of concept for the ability to reproduce the order parameters' time series, approximately equal to equation (13) and (14). The dynamical system studied is described in the form of a generalised Langevin-equation (Van Mourik, Daffertshofer & Beek, 2006; Van Mourik, Daffertshofer & Beek, 2006):

$$\dot{\rho} = f(\rho) + g(\rho)\Gamma(t). \tag{17}$$

Equation (17) displays the evolution of the order parameter (i.e. the derivative of ρ with respect to time t) with deterministic ($f(\rho)$) and stochastic ($g(\rho)\Gamma(t)$) components, which provides insight into the development of frequencies over time. The deterministic components correspond to the intrinsic forces caused by the interactions between oscillators. The stochastic forces, which incorporate the randomness of the oscillators' natural frequencies, initial phases and the external noise, are induced by stochastic force ξ , but are not included in this analysis (Daffertshofer, 2010; Van Mourik et al., 2006; Van Mourik et al., 2006).

To be able to reconstruct the deterministic dynamics and to reproduce the order parameters' time series, as described by Martens et al. in equation (15) and (16), the drift coefficient $D^{(1)}$ is identified, for both ρ and ψ . The aim thereby is to create two two-dimensional (ρ and ψ) polynomial functions to model the dynamical system and to analyse the qualitative characteristics of the system. The claim for these functions to be polynomial is deduced from equations (13) and (14), which show polynomial functions apart from the trigonometric terms. $D^{(1)}$ represents the first Kramers-Moyal coefficient in the dynamics of the corresponding probability density (Daffertshofer, 2010). The Kramers-Moyal coefficients, can be computed by:

$$D^{(k)}(x) = \lim_{\Delta t \rightarrow 0} \frac{1}{\Delta t} \frac{1}{k!} \int (x - x')^k p(x, t + \Delta t | x', t) dx' \tag{18}$$

Hereby, $D^{(1)}$ is identical to the first order cumulant, and Δt represents an infinitesimal time step as the limit approaches zero. To extract this coefficient from the data, first, the data was binned into a range of values associated with each variable. Thereby, the data is divided into equally spaced parts (bins). The assumption holds, that at time t' , the previous sample was present in a bin with centre x' , which relates to a future sample at time t , being present in a bin with centre x ($t > t'$). This method is performed by computing the conditional probability density ($p(x, t | x', t')$), that has to be executed for each combination of bins and all adjacent pairs of samples (Daffertshofer, 2010).

The polynomial functions describing the drift coefficient ($D^{(1)}$), can be of multiple orders. To be able to reproduce the dynamical system as described in equation (13) and (14), it is shown that, after simplifying both equations, the polynomial function consists of coefficients $b\rho$ and $d\rho^3$. In accordance with equation (14), after simplifying, it is shown that the parameters comprise: $b = \frac{\kappa}{2} - \Delta$ and $d = -\frac{\kappa}{2}$.

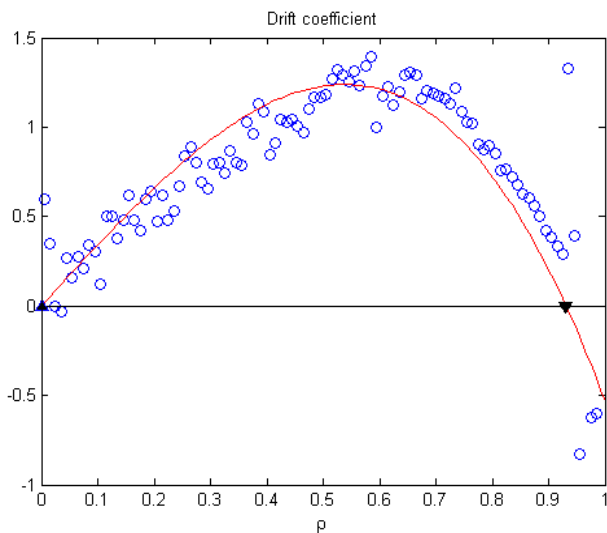


Figure 6: Drift coefficient (blue dots), according to equation (15) and (16) and a polynomial fit (red line), for $\omega_0 = 0$ and $\kappa = 10$, showing an unstable fixed point (upward pointing triangle) and a stable fixed point (downward pointing triangle). As κ is large, a stable fixed point appears for a high value of ρ , showing almost full synchronization of the dynamical system.

To illustrate the proper functioning of the above described method in the case of $\omega_0 = 0$ representing the conventional Kuramoto model, the drift coefficient for $\kappa = 10$, is shown in figure 6. Unstable and stable fixed points are displayed as triangles, pointing upwards or downwards, respectively. The figure shows a stable fixed point at a high value of ρ , indicating almost full synchronization of the dynamical system for this κ -value. Because $\kappa_c = 1$ in the unimodal situation, this topological outline of the system was expected.

Model comparison

The coefficients of the polynomial function are based on the paper of Martens et al., displayed in equation (13) and (14). If these equations however would not have been known, a model comparison method could have been applied to test for which order of the polynomial function would fit best to the data. Despite the knowledge of the coefficients from the paper of Martens et al., a model comparison is applied to test for

this. Two well-known information criteria include the Akaike Information Criteria (AIC) and the Bayesian Information Criteria. The equations belonging to the two comparison methods comprise:

$$\text{AIC} = -2 \ln \mathcal{L}(\hat{\theta}) + 2p; \tag{19}$$

$$\text{BIC} = -2 \ln \mathcal{L}(\hat{\theta}) + p \ln n. \tag{20}$$

Hereby, $\mathcal{L}(\hat{\theta})$ is the likelihood of the estimated model given the model residuals, with $\hat{\sigma}^2$, the maximum likelihood estimate for the variance of the error term distribution, p gives the total number of parameters that are estimated in the model (including σ^2 for general linear models), and n represents the sample size. They all include the same goodness-of-fit term, but the BIC has a more stringent penalty term than the AIC. The goodness-of-fit term is measured by the maximized likelihood and this is overall balanced by the simplicity of the model, as referred to by the dimension p , of the fitted model parameter space. In all criteria, the smaller the outcome, the better the model represents the true data (Aho, Derryberry, & Peterson, 2014; Ward, 2008).

The Kullback-Leibler information (KL-information or KL-divergence) $I(f, g)$, is used to determine the information that is lost when comparing the true model $f(x)$ with an approximating model $g(x|\theta)$, where θ defines the model space (Burnham, Anderson, 2004). In the approximating model the parameters are known. For discrete probability models, the KL-information is defined as:

$$I(f, g) = \sum_x f(x) \ln \left[\frac{f(x)}{g(x|\theta)} \right]. \tag{21}$$

When comparing models, the best model will lose the least information with respect to the true data relative to the other candidate models. This is equivalent to minimizing $I(g, f)$ over $f(x)$. $I(g, f)$ requires knowledge about the true data set and parameters in the candidate models, and is therefore not directly applicable in model selection. The model parameters must be estimated by minimizing the expected estimated KL-information, using the maximum likelihood estimator (MLE) (Aho et al., 2014; Burnham, Anderson, 2004). The expectations with respect to the true model is denoted by the following equations in the case of discrete data:

$$I(f, g) = E [\log(f(x))] - E [\log(g(x|\theta))]. \tag{22}$$

Here, $E [\log(f(x))]$ is a constant across the analysis of models and therefore this part does not depend on the true data or the model. Only the relative expected part of the KL-information ($E [\log(g(x|\theta))]$), needs to be estimated for each candidate model (Burnham, Anderson, 2004).

The decision of which model comparison method to choose has proven to be difficult considering both criteria answer different questions. The AIC is applied to compare non-nested models and models based on different probability distributions. In the AIC, the unknown parameters are estimated by maximizing the likelihood function $g(x|\theta)$ over the parameter space. This function evaluates the conformity of the model to the observed data, by searching among a collection of candidate models $\mathcal{F} = \{\mathcal{F}(k_1), \mathcal{F}(k_2), \dots, \mathcal{F}(k_L)\}$, for the fitted model $g(x|\hat{\theta})$, with $k \in \{k_1, k_2, \dots, k_L\}$. This fitted model serves as the 'best' approximation to the true data $f(y)$ (Aho et al., 2014).

The AIC chooses the most complex model as the sample size increases (efficient method), which will best predict the future sample. This causes the chance of imprecise modeling and tapering effects. The preference of the AIC to choose the most complex model is a disadvantage. The value of the criterion can decrease as the number of parameters in the fitted model is increased, which causes the fitted model to be either correct or overfitted. Thus, when the complexity of the observed data increases, the model that is more capable of adapting to the data, referring to the most complex model, will be chosen.

An important characteristic of the AIC is asymptotic efficiency, which minimizes the prediction error according to the Kullback-Leibler discrepancy between the generating model and the fitted approximating model. Therefore, the AIC maximizes predictive accuracy. When a generating model is of an infinite dimension and therefore lies outside the candidate collection, an asymptotically efficient criterion will asymptotically select the fitted candidate model which minimizes the mean squared error of prediction. With the AIC, overfitting gives a model that will have a lot of random noise, while underfitting provides a model that will be biased when used for future prediction (Aho et al., 2014).

The BIC is an asymptotic, unbiased, large-sample approximation of the Bayes factor, thereby assuming equal priors on candidate models. The model which is a posteriori most probable, will be selected. The method is based on a multivariate normal distribution centered on the MLE, and does not require the specification of priors. The Bayes factor represents the ratio of the posterior probability of the candidate

models. The minimum value of the BIC is in accordance with the highest Bayesian posterior probability (Aho et al., 2014; Burnham, Anderson, 2004).

With increasing sample size, the probability of the best model increases to one, and the probability of the other models decreases to zero. There is therefore a clear target model that the BIC is looking for, although this does not automatically mean this model is the true model (Burnham, Anderson, 2004). When the sample size is smaller than 7.4, the BIC assigns more weight to complex models than the AIC does, but as the sample size increases, the BIC assigns more weight to simpler models in comparison to the AIC (Ward, 2008). For small sample sizes, the model selected by the BIC may be much more parsimonious in comparison to the selected model of the AIC. The BIC-selected model may thus be underfitted with a small sample size and performs better with large sample sizes (Aho et al., 2014; Burnham, Anderson, 2004).

The Bayes' Theorem describes the joint posterior of M_k and θ_k :

$$h((k, \theta_k) | x) = \frac{\pi(k) f(\theta_k | k) L(\theta_k | x)}{m(x)}, \quad (23)$$

with $m(x)$ representing the marginal distribution of x , $\pi(k)$ ($k \in \{k_1, k_2, \dots, k_L\}$) is the discrete prior over the candidate models and $f(\theta_k | k)$ is the prior on θ_k . When the sample size increases, the chance of choosing the correct model increases (Aho et al., 2014; Burnham, Anderson, 2004). To choose between two models, M_{k_1} and M_{k_2} , a Bayes factor is often applied. The Bayes factor: $B12$, is defined as the ratio of the posterior odds of M_{k_1} : $\frac{P(k_1 | y)}{P(k_2 | y)}$, to the prior odds of M_{k_1} : $\frac{\pi(k_1)}{\pi(k_2)}$. If $B12 > 1$, model M_{k_1} is favored by the data, and if $B12 < 1$, model M_{k_2} is favored by the data (Burnham, Anderson, 2004; Ward, 2008). When more than two models are being compared, and all models have equal prior weight, the Bayes factor of model k becomes:

$$BF = \frac{P(x | M_k)}{\sum_i P(x | M_i)}. \quad (24)$$

This is a computationally intensive approach with the difficulty of specifying prior distributions. Bayes factors are known to be unstable and sensitive to the choice of priors. In applying the BIC, it is therefore essential to choose proper priors (Ward, 2008).

The BIC is a consistent criterion, meaning that it will asymptotically select the fitted candidate model with the correct structure and probability one, as the sample size increases. This selected model can be biased at small sample sizes as an estimator of its target model (Aho et al., 2014; Burnham, Anderson, 2004). The differences between the AIC and BIC will be especially pronounced in large sample settings.

The BIC refers to conformation/falsification whereby it is expected to find the correct model, as sample size increases and the process that generates the data is relatively simple (consistent method). Hypothesis testing with precisely specified models of low dimension are therefore required in the BIC (Burnham & Anderson, 2004). As the sample size increases, both criteria will work better, but with different goals. For the AIC, predictive power increases when the model and sample size are large. The BIC, on the other hand, chooses a fixed complexity with increased sample size, but then has a larger probability of selecting the true model. With the AIC, overfitting leads to a model that will have a lot of random noise, while underfitting provides a model that will have a bias when used for future prediction (Aho et al., 2014).

The above mentioned criteria can be divided into two groups, as stated by Ward (2008): "generalization-based criteria", and "explanation-based criteria". Generalization-based criteria (AIC) aim to find the best model that fits both current data and potential future data from the same generating process. Explanation-based criteria (BIC) try to identify the generating process, without influence of potential future data (Ward, 2008).

As argued above, both criteria have distinct pros and cons. Therefore, both have been applied in a model comparison analysis in all three datasets included in this study. The polynomial models that were compared are shown in table 2.

Table 2: Polynomial models included in the AIC and BIC model comparison methods.

Model 1:	$f_1(\rho) = a\rho + b\rho^2$
Model 2:	$f_2(\rho) = a\rho + b\rho^3$
Model 3:	$f_3(\rho) = a\rho^2 + b\rho^3$
Model 4:	$f_4(\rho) = a\rho + b\rho^2 + c\rho^3$

2.1.2 Oscillators' dynamics

In the second part of this study, a dataset was numerically simulated by performing simulations of the conventional Kuramoto model (equation (4)), with multiple values for ω_0 and Δ to create uni- and bimodal frequency distributions. Table 3 lists the parameter settings that were applied in these numerical simulations. In contrast to the simulations of the order parameters' dynamics, in this part of the study, φ 's were simulated. A wide view on the behaviour of the dynamical system was created by drawing φ from a von Mises distribution that ensured the initial ρ -values to cover the range $[0, 1]$. This is defined as perturbations existing of sequencing initial conditions, acting as random perturbations in the concatenated data, resulting in distinct transient behaviour. The correct amount of perturbations depends on both the strength of the noise and the amount of data points. The correct balance between these components had to be found, including sufficient perturbations to be able to analyze the reaction of the system, without reaching a 'stable value' too quickly. The Δ -values describe the width of the distribution(s). ω_0 defines the initial condition of the natural frequencies, and as stated by Martens et al. (2009), $\omega_0 > \frac{\Delta}{\sqrt{3}}$ for the distribution to be bimodal. κ defines the coupling strength of the network, where according to Strogatz (2000), in the unimodal situation: $\kappa_c = \frac{2}{\pi g(0)}$ and $g(\omega) = \frac{\Delta}{\pi(\Delta^2 + \omega^2)}$. To improve statistical accuracy, the simulations were repeated eight times.

Table 3: Parameter settings for the numerical simulations of the oscillators' dynamics

Parameter	Setting
N	10 000
# nodes	500
T	25
ω_0	$(0: .1: 3) * \frac{\delta_0}{\sqrt{3}}$
Δ	$\frac{(0:2)}{2}$
α	$(0: .1: 3)^3$
κ	$(0: 0.05: 5)$
Δt	$\frac{5}{1000}$
Initial Values of φ	100

Because of the finite number of φ 's in these simulations, the equation for the order parameter comprises:

$$\rho(t) = \frac{1}{N} \left| \sum_j e^{i\varphi_j(t)} \right|, \tag{25}$$

with φ representing the phase of an oscillator at time t , and ρ is the order parameter.

To solve the differential equation of the Kuramoto model, a fourth-order Runge-Kutta numerical integration with adaptive step size was applied.

The asymptotic solution (last 100 samples) of ρ is applied in a bifurcation analysis. The dynamics will not reach a stable point but will fluctuate near the end of the simulation (synchrony or asynchrony). This can be explained by the thermodynamic limit which occurs in data with finite sizes, and causes finite size effects. This behaviour resembles erratic motion and is therefore considered as noise in this dataset.

System identification

Subsequently, a system identification approach is applied, as is extensively described in section 2.1.1, to extract the deterministic components from the oscillators' time series and to deduct polynomial functions to describe the data. By performing a bifurcation analysis and comparing the qualitative behaviour of the order parameters' and oscillators' dynamics, it can be verified whether the proposed method by Martens et al. is also applicable to this data set.

Model comparison

As previously described in section 2.1.1, a model comparison has been applied to both numerically simulated data sets in this study. In the oscillators' dynamics, the goal of the model comparison is to check whether the polynomial functions (equation (13) and (14)) are also applicable to this data set.

2.2 Empirical data

In the third part of this study, PD resting-state MEG data was obtained from the VU medical center Amsterdam. The main goal was to assess the applicability of the previously described bimodal frequency distribution (see section 2.1.1) of the Kuramoto model to empirical data. The analyzed data was selected and used in a previous study by Olde Dubbelink et al. (2013), which comprised a longitudinal study cohort (Olde Dubbelink et al., 2013).

Subjects

At baseline, 70 idiopathic PD patients and 21 healthy controls, age-matched to the de novo (early stage) patients, were included in the study. Patients were subdivided into groups according to their disease duration, i.e. 18 recently diagnosed, de novo untreated patients, 19 mild PD patients (disease duration 3-5 years), a group of mild-moderate PD patients (N=16, disease duration 6-8 years) and a group of moderate PD patients (N=17, disease duration 9-11 years). The latter three groups comprise 37 PD patients with levodopa-treatment. Controls were age-matched to PD patients in all groups. Follow-up measurements after 4.3 ± 0.8 (mean \pm standard deviation) years were completed by 59 PD patients and 16 controls.

Disease duration was defined by the patients' subjective estimate of the onset of the first motor symptoms. Additional subject characteristics as described by Olde Dubbelink and co-workers include: the Unified Parkinson's Disease Rating Scale motor ratings (UPDRS-III) obtained in the 'ON' medication state; the Cambridge Cognitive Examination (CAMCOG) scale for global cognitive functioning and presence of dementia; and daily dose of levodopa. Thereby, a specific neuropsychological evaluation has been performed including three tasks from the Cambridge Neuropsychological Test Automated Battery (CANTAB) and the Vienna perseveration task (VPT) was conducted to measure perseverance in generating random motor behaviour (Olde Dubbelink et al., 2013).

MEG data acquisition and pre-processing

MEG data were acquired as previously described by Olde Dubbelink and co-workers using a 151-channel whole-head radial gradiometer MEG system. A recording band pass was set at 0.25-200 Hz with a sample rate of 312.5 Hz. MEG data was recorded for five minutes in an eyes-closed, resting-state condition. Patients treated with levodopa were recorded in the 'ON' medication state. The data was divided into epochs of 4096 samples of which four artifact-free epochs were selected. Due to different technical problems 12 of the original 151 channels were excluded. For further analysis, the epochs were converted to ASCII-files and imported into the BrainWave software package (see Olde Dubbelink et al., 2013 for details).

MEG sensor signals were projected to an anatomical framework consisting of 78 cortical regions by an atlas-based beamforming approach. Time series of 6 frequency bands (delta (0.5-4 Hz), theta (4-8 Hz), alpha1 (8-10 Hz), alpha2 (10-13 Hz), beta (13-30 Hz) and gamma (30-48 Hz)) were subsequently estimated to determine neural activation. Eventually six sets of 78 time-series were conducted.

Data analysis

The PD MEG data is first filtered from the alpha1 to the beta frequency band (8-30 Hz) using a second order Butterworth band pass filter. To extract the phases of the MEG data, the Hilbert transform is applied and the global order parameter (ρ) is calculated. Subsequently, to be able to calculate ψ , the data was filtered, again with a second order butterworth band pass filter, to the alpha1 (8-10 Hz) and beta (20-30) frequency band. Thereafter, the order parameters ρ_1 and ρ_2 for both groups of oscillators (alpha1 and beta) were determined and the average phase difference (ψ) between the groups was calculated. ρ and ψ are subsequently applied in the analysis as set up in paragraph 2.1.1, including a system identification approach and bifurcation analysis to analyze the dynamics of the empirical data. The aim thereby is to look for the simultaneous changes in alpha1 and beta frequency and whether this can be modelled by applying a bimodal frequency distribution to the Kuramoto model of coupled phase oscillators. A bifurcation analysis of the system will show whether this method is applicable to the PD MEG data and whether it is beneficial in comparison to the unimodal frequency distribution of the natural frequencies.

3 Results

3.1 Numerical analysis

3.1.1 Order parameters' dynamics

The system identification approach was successfully applied to numerical simulations of equation (15) and (16), as is displayed in figure 7 and 8. A proof of concept for the ability to reproduce the results of the paper by Martens and co-workers is displayed in figure 7A and C, where the asymptotic solutions of the order parameter are similar to the zero crossings of the drift coefficient. It was therefore decided to continue the analysis according to the proposed method (section 2.1.1).

Equation (15) and (16) are composed of a deterministic and stochastic part. $\overline{D^{(1)}}$ is extracted for ρ and ψ , representing vector field: $\begin{pmatrix} D_{\rho}^{(1)} \\ D_{\psi}^{(1)} \end{pmatrix}$. In equation (16) the stochastic part is equal to zero (for a more detailed description see section 2.1.1). Therefore, in the system identification approach, equation (15) and (16) can be rewritten into:

$$\dot{\rho} = D_{\rho}^{(1)}(\rho, \psi) + D_{\rho\rho}^{(2)}(\rho, \psi) \quad (26)$$

$$\dot{\psi} = D_{\psi}^{(1)}(\rho, \psi) \quad (27)$$

Thereby, as previously described in section 2.1.1, only $D^{(1)}$ is included for further analysis of the system.

Because ψ is defined by the phase difference between the two Lorentzian distributions that are included in the bimodal model, in the unimodal situation when $\psi = 0$, $D_{\rho}^{(1)}(\rho, \psi)$ describes the qualitative behaviour of the system. In the bimodal situation, when ψ can exhibit any value, both $D_{\rho}^{(1)}(\rho, \psi)$ and $D_{\psi}^{(1)}(\rho, \psi)$ are taken into account.

The asymptotic solutions of ρ , represented in figure 7A and C, show different behaviour in the unimodal and bimodal situation. In the unimodal situation, the asymptotic solutions resemble the theoretical behaviour of the order parameter as described by Strogatz (2000), while in the bimodal situation, the asymptotic solutions show deviations of this behaviour between $\kappa = 2$ and $\kappa = 5$. Thereby, κ_c shifted from 1 in the unimodal situation, to 2 in the bimodal situation. However, both systems stabilize at a certain point.

Figure 7B and D represent the overall behaviour of the dynamical system in the unimodal and bimodal situation, respectively, including $D_{\rho}^{(1)}(\rho, \psi)$ and a null cline representing the zero-crossings of $D_{\rho}^{(1)}(\rho, \psi)$.

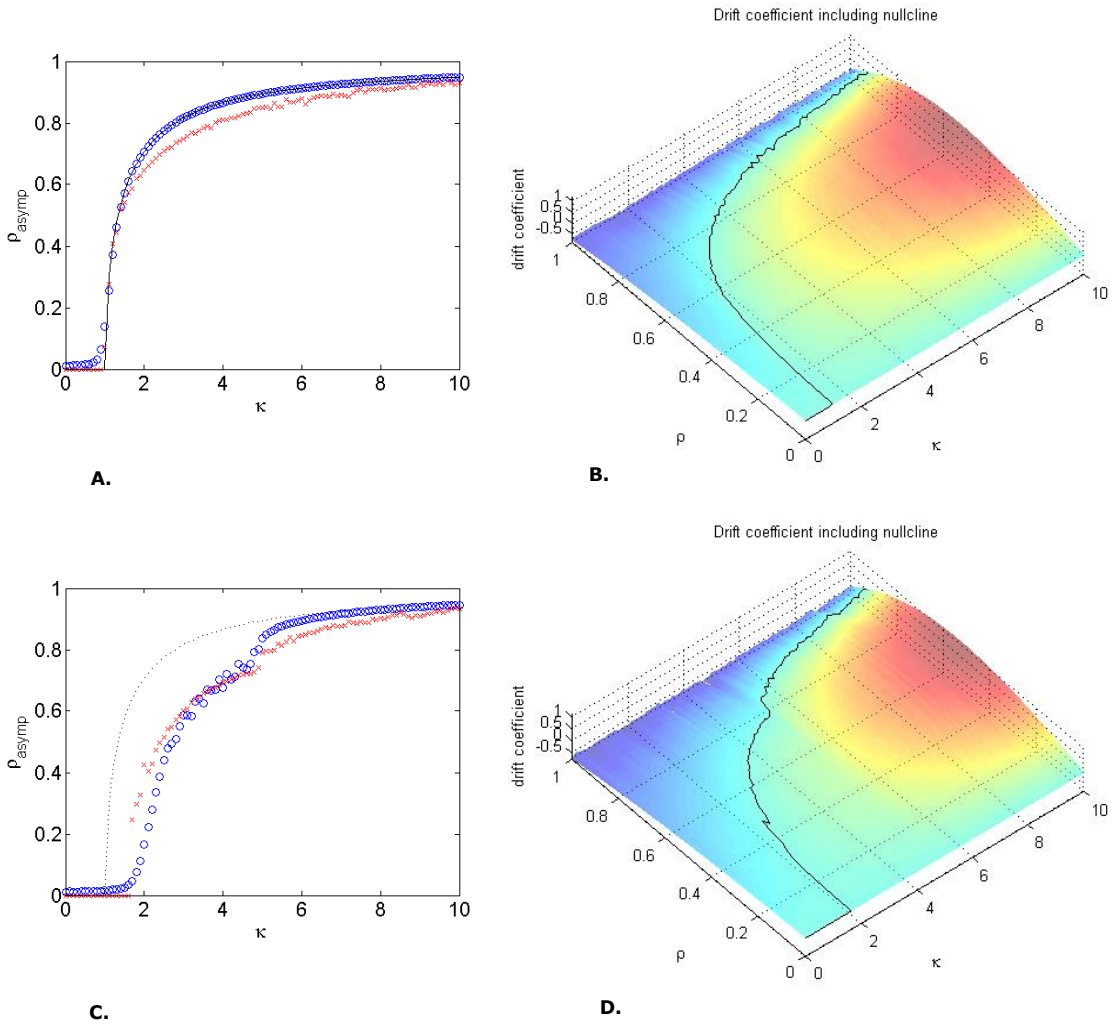


Figure 7: Numerical simulations of equation (15) and (16) **A & C:** Influence of the coupling strength on synchronization. The asymptotic solutions of ρ are represented by the blue dots and the red crosses denote the zero-crossings of $D_\rho^{(1)}(\rho, \psi)$, both dependent on coupling strength κ . **A:** Unimodal situation: $\omega_0 = 0$. The black line represents the theoretical behaviour of ρ . The similarity in the asymptotic solutions of ρ and the zero crosses of $D_\rho^{(1)}(\rho, \psi)$ provide a proof of concept for the ability to reproduce the results by the paper of Martens et al.. **C:** Bimodal situation: $\omega_0 = 2$. The dotted black line is plotted to display the deviations in this situation of the asymptotic solutions of ρ and the zero crossings of the $D_\rho^{(1)}(\rho, \psi)$. Note: $\kappa_c = 1$ when $\omega_0 = 0$ and $\kappa_c = 2$ when $\omega_0 = 2$. **B & D:** Total topological outline of $D_\rho^{(1)}(\rho, \psi)$ for each κ - and ρ - value including a polynomial fit of the zero crossings of $D_\rho^{(1)}(\rho, \psi)$ represented by the black line. **B:** Unimodal situation: $\omega_0 = 0$. **D:** Bimodal situation: $\omega_0 = 2$.

Figure 8 shows results of $D_\rho^{(1)}(\rho, \psi)$ for three different κ -values. Stable fixed points (referring to synchronization/desynchronization of the system) are equal to the zero-crossings where the derivative of $D_\rho^{(1)}(\rho, \psi)$ has a negative slope, whereas unstable fixed points are appointed by a positive slope of the derivative. When comparing the unimodal to the bimodal situation in figure 8, it is shown that the topological outline of both systems do not differ qualitatively for all displayed κ -values. The polynomial fit however, deteriorates in the bimodal situation.

Figure 7 and 8 confirm that, as described by the conventional Kuramoto model, when $\kappa < \kappa_c$, there is no synchronization of the system, and when $\kappa > \kappa_c$ the system starts to synchronize. This is applicable to both the uni- and bimodal situation.

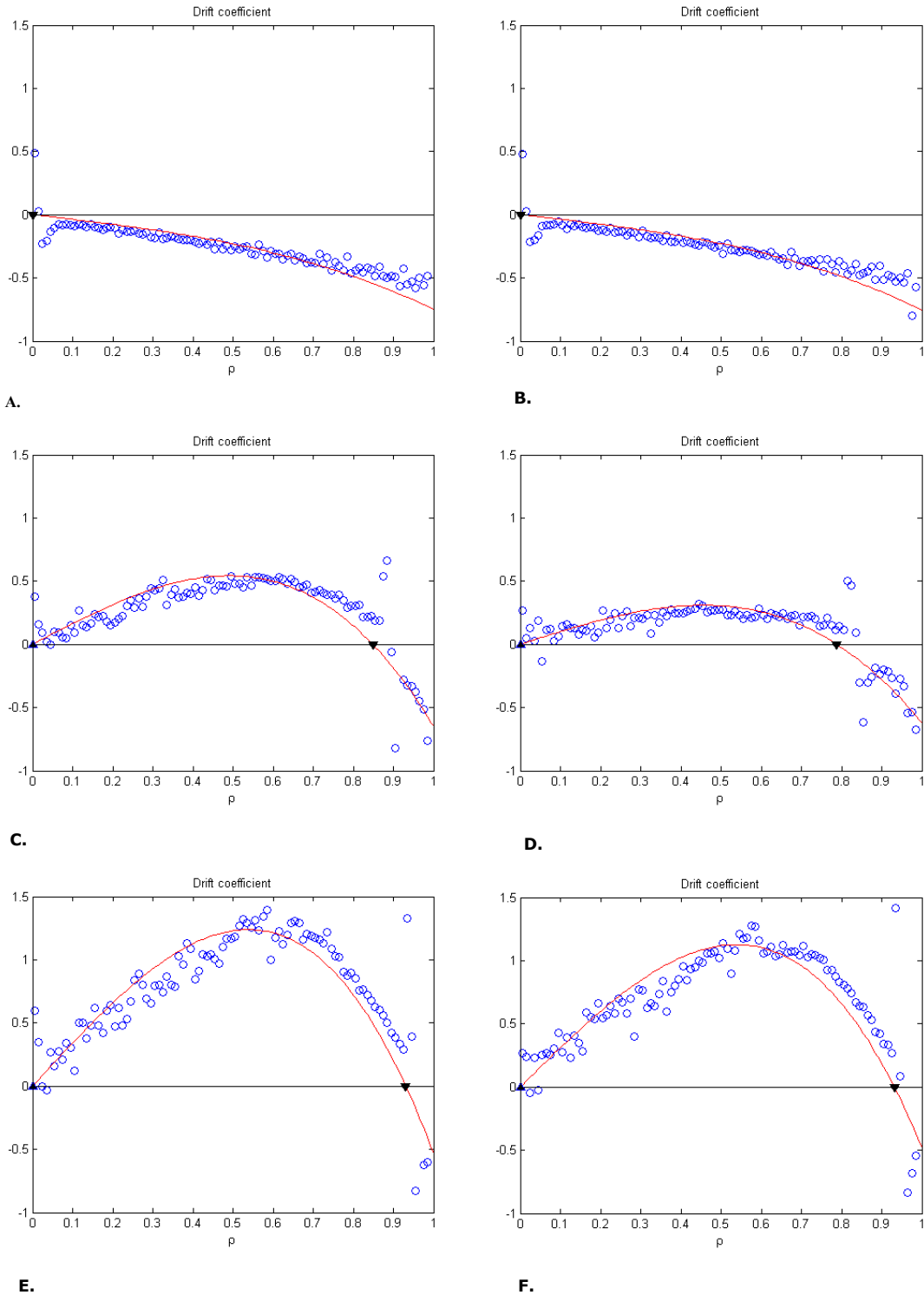


Figure 8: $D_{\rho}^{(1)}(\rho, \psi)$ (blue dots) with a polynomial fit (red line) including unstable fixed points (triangle pointing upwards) and stable fixed points (triangle pointing downwards). The stable fixed points are appointed by the zero crossings of the polynomial fit where the derivative of $D_{\rho}^{(1)}(\rho, \psi)$ is negative. The unstable fixed points are appointed by the zero crossings of the polynomial fit where the derivative of $D_{\rho}^{(1)}(\rho, \psi)$ is positive. **A:** Unimodal situation: $\omega_0 = 0, \kappa = 0$. **B:** Bimodal situation: $\omega_0 = 2, \kappa = 0$. **A & B:** As $\kappa < \kappa_c$ an unstable fixed point appears for a very low value of ρ , representing asynchrony in the dynamical system. **C:** Unimodal situation: $\omega_0 = 0, \kappa = 5$. **D:** Bimodal situation: $\omega_0 = 2, \kappa = 5$. **C & D:** As $\kappa > \kappa_c$, a stable fixed point appears for a high value of ρ , representing almost full synchronization of the dynamical system. **E:** Unimodal situation: $\omega_0 = 0, \kappa = 10$. **F:** Bimodal situation: $\omega_0 = 2, \kappa = 10$. **E & F:** As $\kappa \gg \kappa_c$ is large, a stable fixed point appears for a high value of ρ , showing almost full synchronization of the dynamical system.

$D_\rho^{(1)}(\rho, \psi)$ and $D_\psi^{(1)}(\rho, \psi)$ are visualized in figure 9 in the unimodal and bimodal situation. Figure 9B displays that ψ shows nullclines for $0, \pi$ and 2π . Thereby, both the nullcline at 0 and 2π are stable, and the nullcline at π is unstable. The expectation of ψ to be equal to zero in the unimodal situation is therefore confirmed (see equation (16)). This analysis confirms the stable fixed points that are visualized in figure 8. Furthermore, when combining both figures for $D_\rho^{(1)}(\rho, \psi)$ and $D_\psi^{(1)}(\rho, \psi)$, fixed points of the bimodal system can be localized. When the nullcline of both $D_\rho^{(1)}(\rho, \psi)$ and $D_\psi^{(1)}(\rho, \psi)$ are stable and overlap, they indicate the position of a stable fixed point. $D_\psi^{(1)}(\rho, \psi)$ does show values in the bimodal situation, confirming what was expected as described previously.

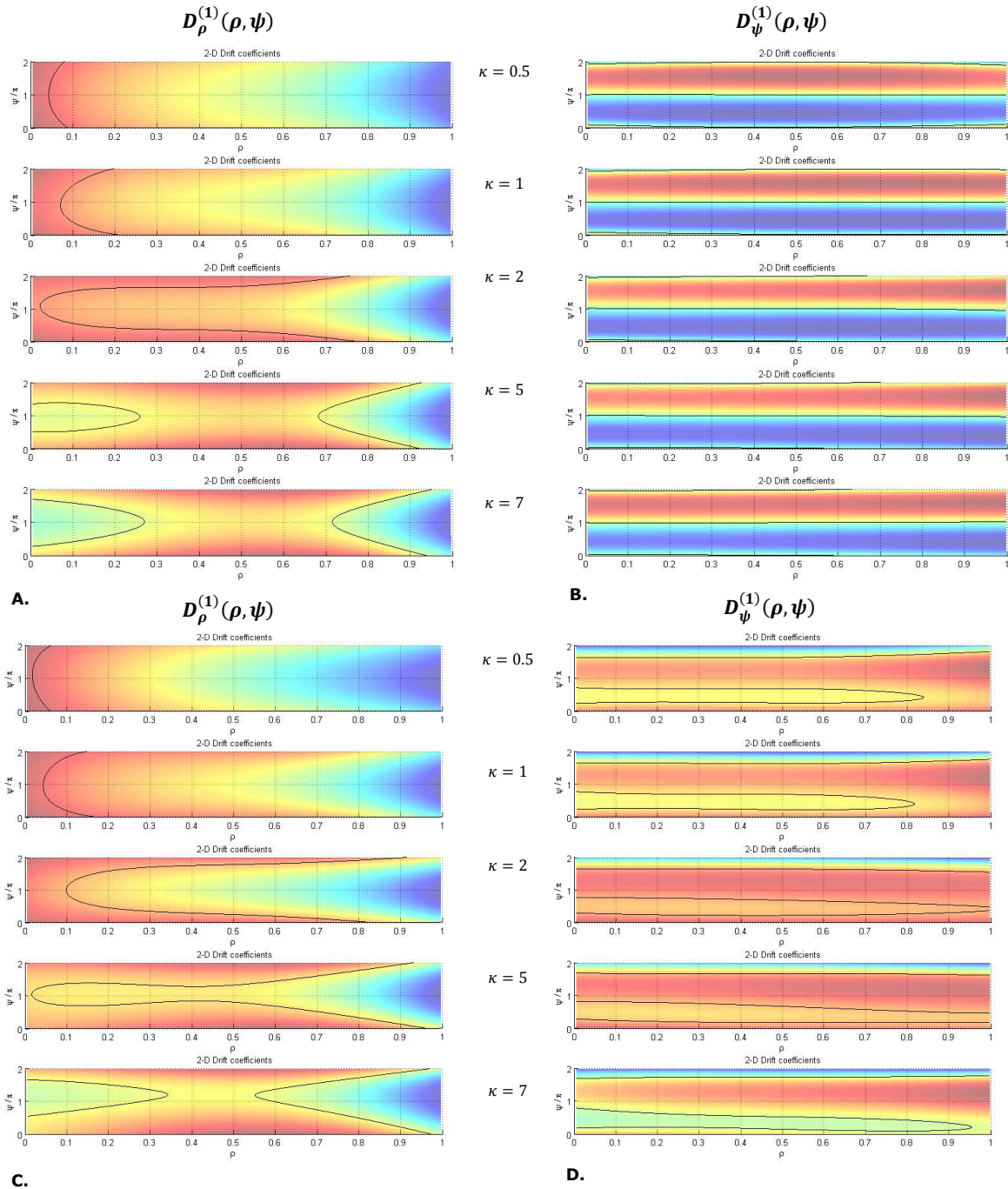


Figure 9: Two-dimensional drift coefficients $D_\rho^{(1)}(\rho, \psi)$ (**A** and **C**) and $D_\psi^{(1)}(\rho, \psi)$ (**B** and **D**) plus null clines (black lines) for different κ -values. The null clines are stable when the contour of the figure decreases (negative slope) in height (see colorbar), or are unstable when the contour of the figure increases (positive slope) in height. **A and B:** Unimodal situation ($\omega_0 = 0$). **C and D:** Bimodal situation ($\omega_0 = 2$). **E:** Colour bar indicating the height of the contour colors. When comparing $D_\rho^{(1)}(\rho, \psi)$ in the uni- and bimodal situation no big differences can be seen in the topological outline of the system. For $D_\psi^{(1)}(\rho, \psi)$ however, the figure displays stable null clines for 0 and 2π in the unimodal situation and a more flat topology and different values for the null clines in the bimodal situation.

The polynomial fit as applied to $D_\rho^{(1)}(\rho, \psi)$ is based on equation (13) and (14). Figure 10A and B show the parameters of a polynomial function with $b\rho$ and $d\rho^3$. As applied to the order parameters' times series, 10A and B indicate the accuracy of these parameters in both the uni- and bimodal situation. When a polynomial function with parameters a , $b\rho$, $c\rho^2$ and $d\rho^3$ is applied, its inaccuracy is displayed in figure

10C. By comparing multiple polynomial functions with different parameters by means of a model comparison method, it can be either confirmed or rejected whether the proposed parameters according to equation (13) and (14) are correct.

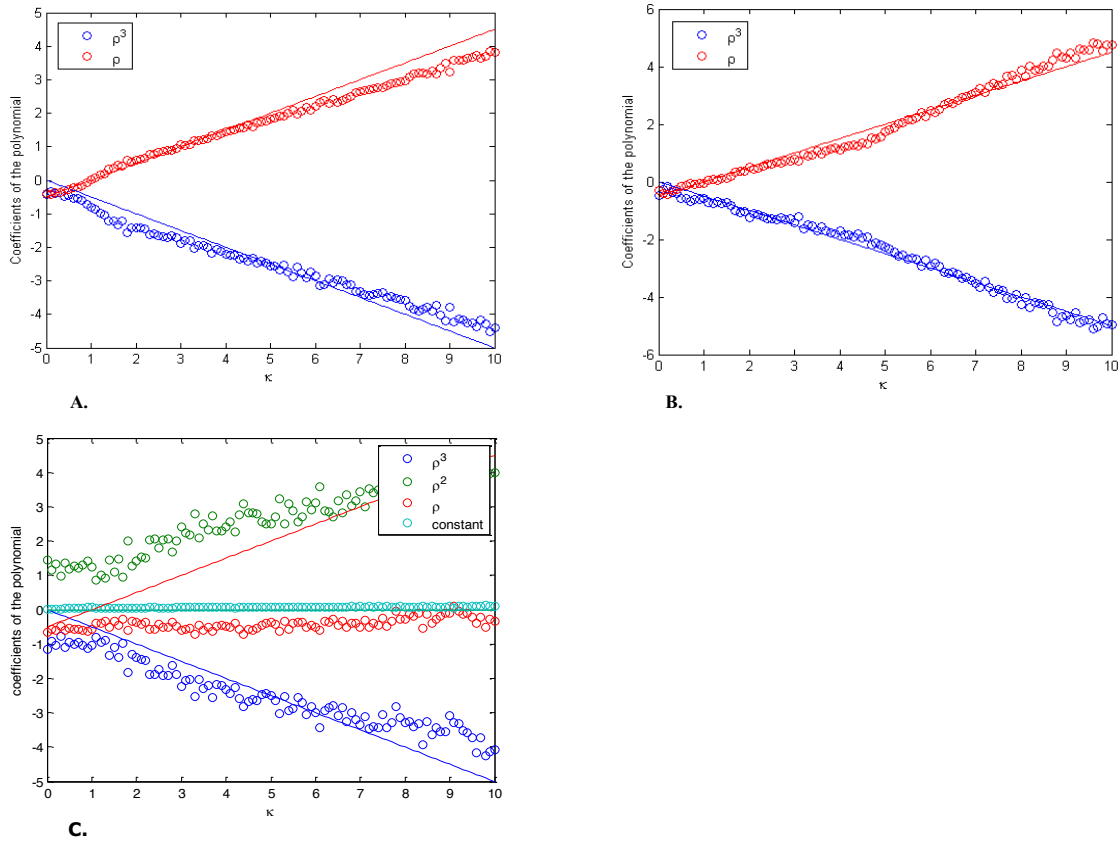


Figure 10: Polynomial functions with different parameters fitted to the uni- and bimodal data to check for the accuracy of the parameters to describe the order parameters' dynamical system. The accuracy is confirmed when the colored dots resemble the equally colored solid lines. **A:** Unimodal data ($\omega_0 = 0$) fitted with a polynomial function with parameters $b\rho$ and $d\rho^3$. **B:** Bimodal data ($\omega_0 = 2$) fitted with a polynomial function with parameters $b\rho$ and $d\rho^3$. **A and B:** Both figures show that in both the uni- and bimodal data the accuracy of these parameters are confirmed. **C:** Unimodal data ($\omega_0 = 0$) fitted with a polynomial function with parameters a , $b\rho$, $c\rho^2$ and $d\rho^3$. The deviations of the colored dots from the equally colored solid lines show the inaccuracy of these parameters.

As described in section 2.1.1, the AIC and BIC are applied to test for which model is the best fit to the uni- and bimodal data and to either reject or confirm the parameters of the polynomial function as proposed by Martens and co-workers.

The models that are included in the model comparison are displayed in table 2 (see section 2.1.1, model comparison). The average AIC and BIC values¹ for each model applied to the order parameters' dynamics are displayed in table 4.

Table 4: AIC and BIC values for each model applied to the order parameters' dynamics, for the uni- and bimodal situation.

Model	$\omega_0 = 0$				$\omega_0 = 2$			
	1	2	3	4	1	2	3	4
Average AIC-value	5,61	4,76	8,79	7,61	5,22	4,49	8,04	7,22
Average BIC-value	32,07	31,22	35,24	42,89	31,68	30,95	34,50	42,50

Table 4 shows that for both the unimodal and bimodal situation, model 2 ($f_2(\rho) = a\rho + b\rho^3$) gives the lowest scores for both the AIC and BIC. While, as described in section 2.1.1, the two methods are hard to compare because they answer different questions, both methods choose the same model to be the best fit to the data. The parameters of the polynomial function as described by Martens and co-workers are thereby confirmed.

¹ The AIC and BIC scores for each κ -value are detailed in appendix B.

3.1.2 Oscillators' dynamics

The system identification approach was successfully applied to numerical simulations of equation (4), as is displayed in figure 11 and 12. Thereby, in accordance with section 3.1.1, $\overline{D^{(1)}}$ is extracted for ρ and ψ .

The asymptotic solutions of ρ , represented in figure 11A and B, show different behaviour in the unimodal and bimodal situation. In the unimodal situation, the asymptotic solutions resemble the theoretical behaviour of the order parameter as described by Strogatz (2000), while in the bimodal situation, the asymptotic solutions show deviations of this behaviour between $\kappa = 1$ and $\kappa = 5$. Thereby, according to the asymptotic solutions of ρ , $\kappa_c = 1$ in the unimodal situation, whereas in the bimodal situation κ_c seems to be equal to 2 although this is not as clear as in the unimodal situation. The zero-crossings of $D_\rho^{(1)}(\rho, \psi)$ however, display another value for κ_c in the bimodal situation, i.e. $\kappa_c = 3$. The difference between the zero-crossings of $D_\rho^{(1)}(\rho, \psi)$ and the asymptotic solutions of ρ indicate the inaccuracy of the polynomial fit which is applied to $D_\rho^{(1)}(\rho, \psi)$ and visualized in more detail in figure 12.

When comparing the simulations of the order parameters' dynamics and the simulations of the oscillators' dynamics, the zero-crossings of $D_\rho^{(1)}(\rho, \psi)$ of the order parameters' dynamics (figure 7A and C) follow the same line as the asymptotic solutions of ρ , though in the data of the oscillators' dynamics (figure 11A and C), a deviation of the zero-crossings is visible. This difference is related to the inaccuracy of the polynomial fit as applied to the oscillators' dynamics which was based on the paper of Martens and co-workers. When comparing the bimodal situation of both numerically simulated data sets (figure 7C and 11C), the asymptotic solutions of ρ seem to develop similarly considering the order parameters' dynamics were simulated for $\kappa = 1:0.1:10$ and the oscillators' dynamics for $\kappa = 1:0.05:5$. Thereby, the resolution of κ is equal in both data sets but the absolute values differ.

Figure 11B and D represent the overall behaviour of $D_\rho^{(1)}(\rho, \psi)$ in the unimodal and bimodal situation, respectively. Again, a difference is seen in comparing the bimodal situations of the order parameters' dynamics and the oscillators' dynamics (see figure 7D and 11D). Furthermore, figure 7B and D show that the values of $D_\rho^{(1)}(\rho, \psi)$ for both the uni- and bimodal situation are higher in comparison to the values of $D_\rho^{(1)}(\rho, \psi)$ of the order parameters' dynamics.

The issue regarding the asymptotic solutions of ρ is whether this actually are the asymptotic solutions, or whether the simulations were not recorded long enough and transient behaviour is exhibited. Especially in figure 11C, transient behaviour is likely displayed.

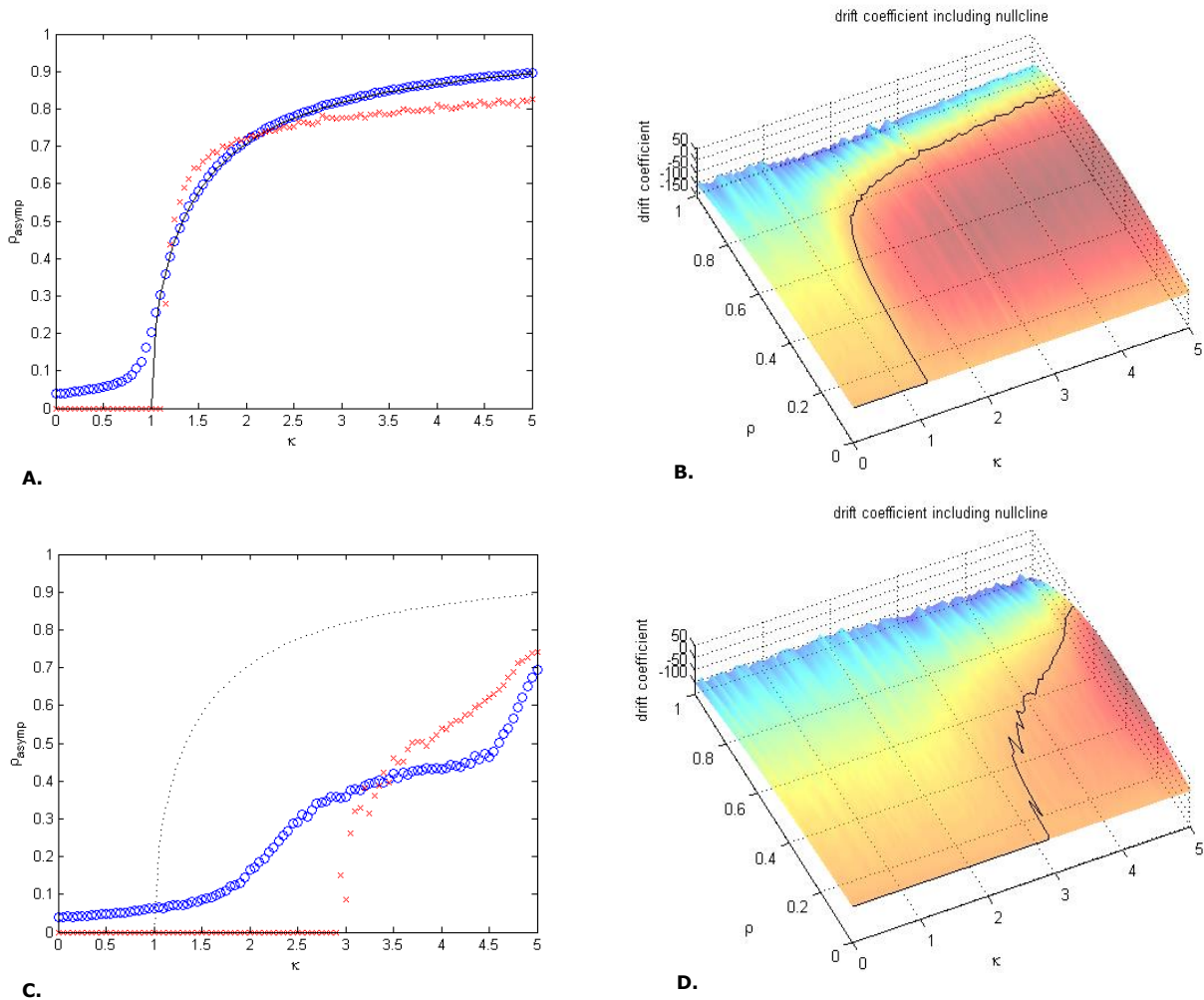


Figure 11: Numerical simulations of equation (4) **A & C:** Influence of the coupling strength on synchronization. The asymptotic solutions of ρ are represented by the blue dots and the red crosses denote the zero crossings of $D_\rho^{(1)}(\rho, \psi)$, both dependent on coupling strength κ . **A:** Unimodal situation: $\omega_0 = 0$. The black line represents the theoretical behaviour of ρ . The difference in the asymptotic solutions of ρ and the zero crossings of $D_\rho^{(1)}(\rho, \psi)$ is related to the applied polynomial function. **C:** Bimodal situation: $\omega_0 = 2$. The dotted black line is visualized to display the deviations of the asymptotic solutions of ρ and the zero crossings of the $D_\rho^{(1)}(\rho, \psi)$ in this situation. Note: $\kappa_c = 1$ when $\omega_0 = 0$ and κ_c does not show a distinct value when $\omega_0 = 2$. **B & D:** Total topological outline of $D_\rho^{(1)}(\rho, \psi)$ for each κ - and ρ - value including a polynomial fit of the zero crossings of $D_\rho^{(1)}(\rho, \psi)$ represented by the black line. **B:** Unimodal situation: $\omega_0 = 0$. **D:** Bimodal situation: $\omega_0 = 2$.

Figure 12 shows results of $D_\rho^{(1)}(\rho, \psi)$ for three different κ -values. When comparing the unimodal to the bimodal situation, it is shown that the topological outline of both systems do not differ qualitatively. As described previously, the polynomial function which is derived from the paper of Martens and co-workers, is not a proper fit as is especially visible in figure 12C, D, E and F.

When comparing $D_\rho^{(1)}(\rho, \psi)$ of the order parameters' dynamics and the oscillators' dynamics, $D_\rho^{(1)}(\rho, \psi)$ of the oscillators' dynamics could deviate from $D_\rho^{(1)}(\rho, \psi)$ of the order parameters' dynamics because this data set is not in a stationary regime or because a polynomial function cannot be fitted to the data. The Ott & Antonsen ansatz as proposed in the paper of Martens and co-workers could thereby be too coarse for this type of data.

When comparing figure 8 to figure 12 it is visualized that the oscillators' dynamics contain less data points in comparison to the order parameters' dynamics.

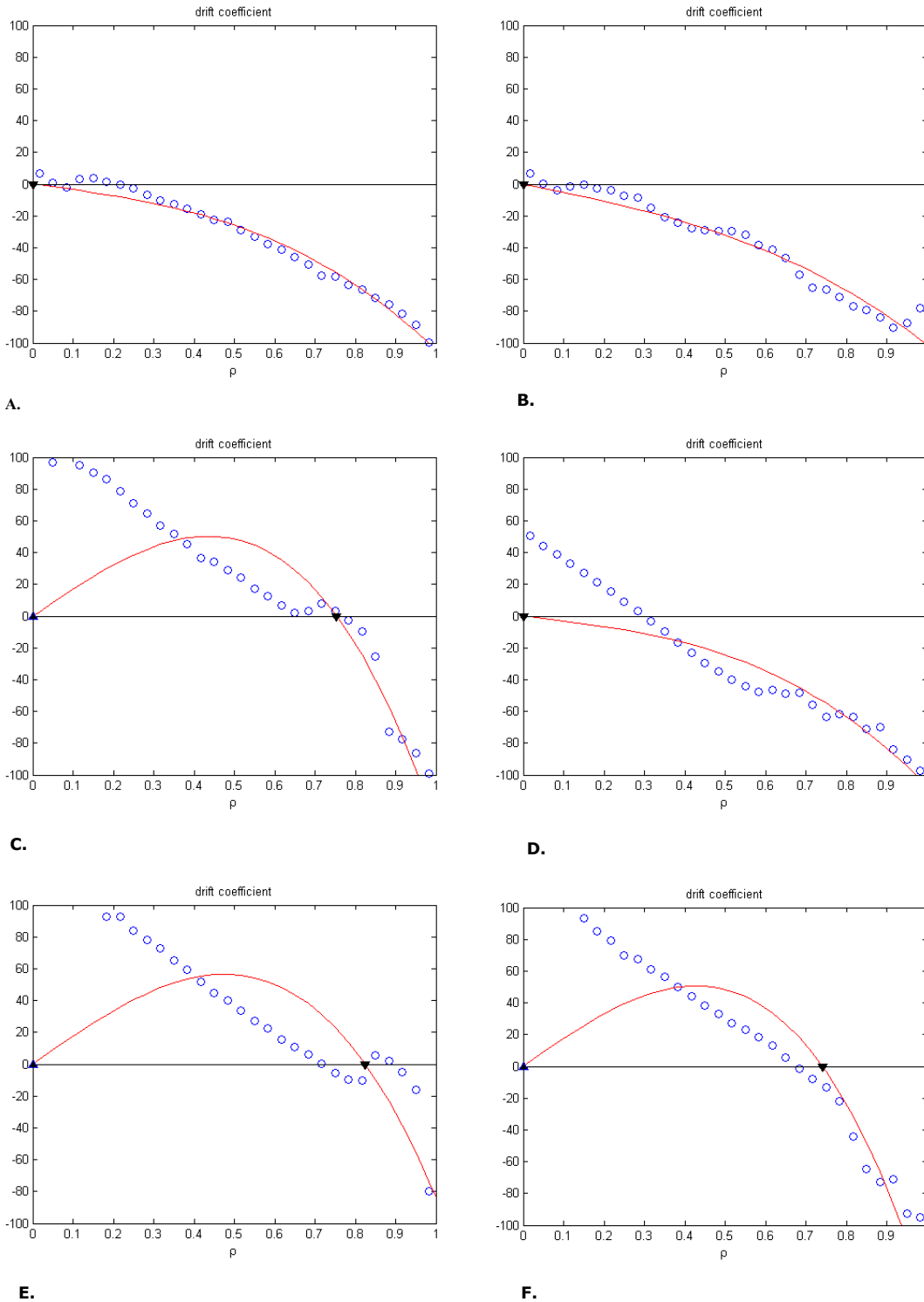


Figure 12: $D_{\rho}^{(1)}(\rho, \psi)$ (blue dots) with a polynomial fit (red line), including unstable fixed points (triangle pointing upwards) and stable fixed points (triangle pointing downwards). The stable fixed points are appointed by the zero crossings of the polynomial fit where the derivative of $D_{\rho}^{(1)}(\rho, \psi)$ is negative. The unstable fixed points are appointed by the zero crossings of the polynomial fit where the derivative of $D_{\rho}^{(1)}(\rho, \psi)$ is positive. **A:** Unimodal situation: $\omega_0 = 0$, $\kappa = 0$. **B:** Bimodal situation: $\omega_0 = 2$, $\kappa = 0$. **A & B:** As $\kappa < \kappa_c$ an unstable fixed point appears for a very low value of ρ , representing asynchrony in the dynamical system. **C:** Unimodal situation: $\omega_0 = 0$, $\kappa = 2.5$. As $\kappa > \kappa_c$, a stable fixed point appears, showing partial synchronization of the dynamical system. **D:** Bimodal situation: $\omega_0 = 2$, $\kappa = 2.5$. Because κ_c could not be appointed in this situation, but $\rho \approx 0.3$, partial synchronization of the system is shown. **E:** Unimodal situation: $\omega_0 = 0$, $\kappa = 5$. **F:** Bimodal situation: $\omega_0 = 2$, $\kappa = 5$. **E & F:** As $\kappa > \kappa_c$, a stable fixed point appears, showing partial synchronization of the dynamical system.

$D_\rho^{(1)}(\rho, \psi)$ and $D_\psi^{(1)}(\rho, \psi)$ are visualized in figure 13 in the unimodal and bimodal situation. Figure 13B displays that ψ shows nullclines different from $0, \pi$ or 2π for $\kappa = 0.5$ and $\kappa = 3$ which deviates from the values of ψ in figure 9B. Thereby, these values are unexpected because in the unimodal situation there is only one population so no phase difference should be present. In the bimodal situation $D_\psi^{(1)}(\rho, \psi)$ does show values, which is similar to $D_\psi^{(1)}(\rho, \psi)$ of the order parameters' dynamics. The topological outline of $D_\rho^{(1)}(\rho, \psi)$ does resemble that of the order parameters' dynamics (as displayed in figure 9A and C) qualitatively. This is also confirmed by combining both figures for $D_\rho^{(1)}(\rho, \psi)$ and $D_\psi^{(1)}(\rho, \psi)$, whereby fixed points of the system can be localized as is previously described in section 3.1.1.

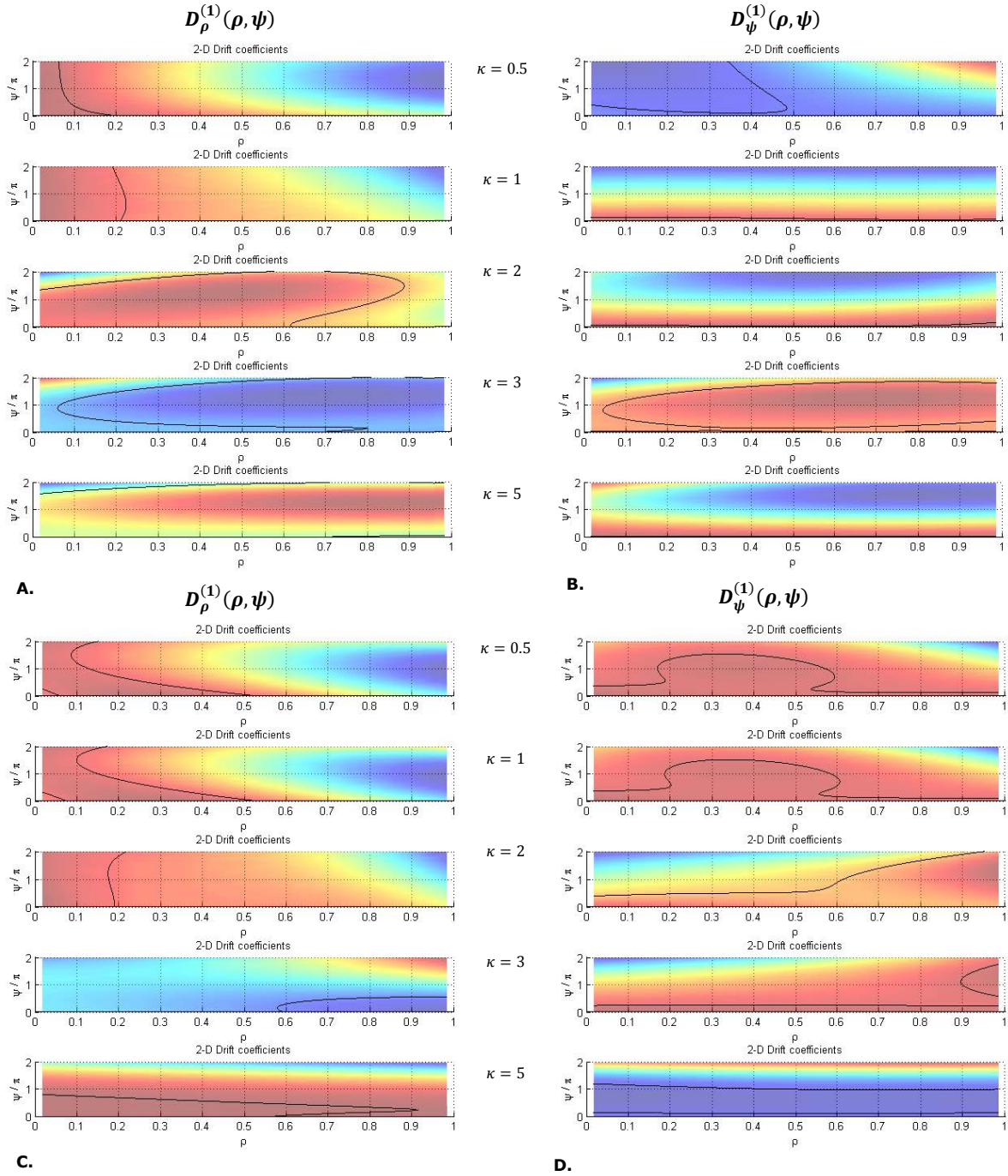


Figure 13: Two-dimensional drift coefficients $D_\rho^{(1)}(\rho, \psi)$ (**A** and **C**) and $D_\psi^{(1)}(\rho, \psi)$ (**B** and **D**) plus nullclines (black lines) for different κ -values. The nullclines are stable when the contour of the figure decreases (negative slope) in height (see colorbar), or are unstable when the contour of the figure increases (positive slope) in height. **A and B:** Unimodal situation ($\omega_0 = 0$). **C and D:** Bimodal situation ($\omega_0 = 2$). **E:** Colour bar indicating the height of the contour colors. When comparing $D_\rho^{(1)}(\rho, \psi)$ in the uni- and bimodal situation no big differences can be seen in the topological outline of the system, although in the bimodal situation the system starts to synchronize for a higher value of κ . For $D_\psi^{(1)}(\rho, \psi)$, the figure displays stable nullclines for 0 and 2π in the unimodal situation for $\kappa = 1, 2$ and 5 and different values for the nullclines in the bimodal situation.

Figure 14A and B show the parameters of a polynomial function with $b\rho$ and $d\rho^3$ as applied to the oscillators' dynamics were also fitted to the order parameters' dynamics. By comparing figure 10 with figure 14 it can be seen that both figures show completely different values for the parameters of the polynomial functions. The polynomial function as proposed by equation (13) and (14) therefore does not seem to be the proper fit to this data set.

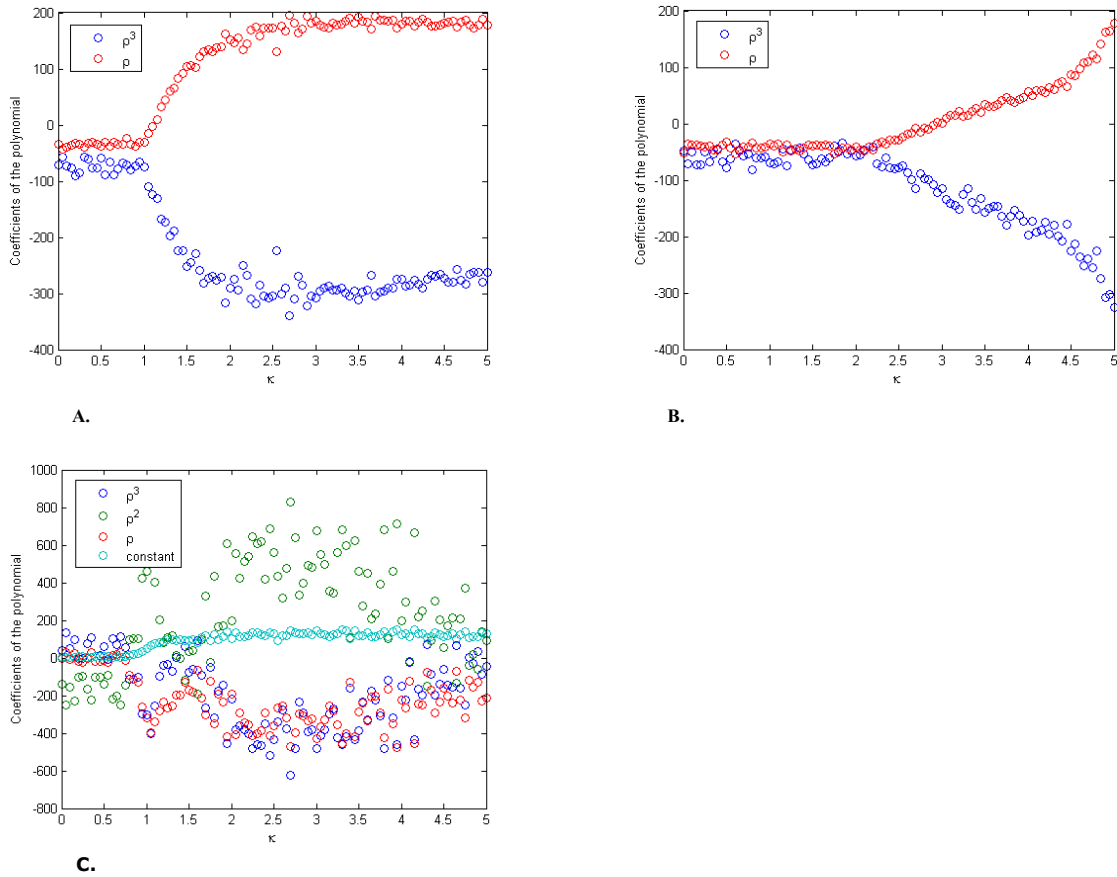


Figure 14: Polynomial functions with different parameters fitted to the uni- and bimodal data to check for the accuracy of the parameters to describe the oscillators’ dynamics. **A:** Unimodal data ($\omega_0 = 0$) fitted with a polynomial function with parameters $b\rho$ and $d\rho^3$. **B:** Bimodal data ($\omega_0 = 2$) fitted with a polynomial function with parameters $b\rho$ and $d\rho^3$. **C:** Unimodal data ($\omega_0 = 0$) fitted with a polynomial function with parameters a , $b\rho$, $c\rho^2$ and $d\rho^3$. When comparing the parameters in this figure to those of the order parameters’ dynamics (figure 14), it is shown that both figures show completely different values for the parameters of the polynomial functions.

As described in section 2.1.1, the AIC and BIC are applied to test for which model is the best fit to the uni- and bimodal data. The AIC and BIC are applied to the oscillators’ dynamics to test whether the proposed polynomial function is also applicable to this dataset.

The models that are included in the model comparison are displayed in table 2. The average AIC and BIC values² for each model applied to the oscillators’ dynamics are displayed in table 5.

Table 5: AIC and BIC values for each model applied to the oscillators’ dynamics as included in the model comparison for the uni- and bimodal situation.

Model	$\omega_0 = 0$				$\omega_0 = 2$			
	1	2	3	4	1	2	3	4
Average AIC-value	15,28	14,47	17,13	17,28	13,86	13,01	15,07	15,86
Average BIC-value	34,83	34,02	36,68	43,34	33,41	32,56	34,62	41,93

Table 5 shows that for both the unimodal and bimodal situation, model 2 ($f_2(\rho) = a\rho + b\rho^3$) gives the lowest scores for both the AIC and BIC. Again, both methods choose the same model to be the best fit to the data and similar to section 3.1.1, both methods choose model 2. The parameters of the polynomial function as described by Martens and co-workers therefore do seem to be the best fit to this data.

² The AIC and BIC scores for each κ -value are detailed in appendix B.

3.2 Empirical data

The bimodal frequency distribution in phase oscillators as described by Martens and co-workers is applied to experimental data to assess its applicability. The experimental data consists of PD resting-state MEG data as described in section 2.2.

According to Olde Dubbelink and co-workers, multiple frequencies change over the course of the disease in PD. The average $\rho(t)$ -value is visualized in figure 15. Here, the average $\rho(t)$ -value does not show a distinct structure of disease progression. Therefore, it will not be meaningful to apply statistics to this measure. Rather, ρ and ψ are analyzed as a dynamical system to qualify changes in synchronisation over the course of the disease.

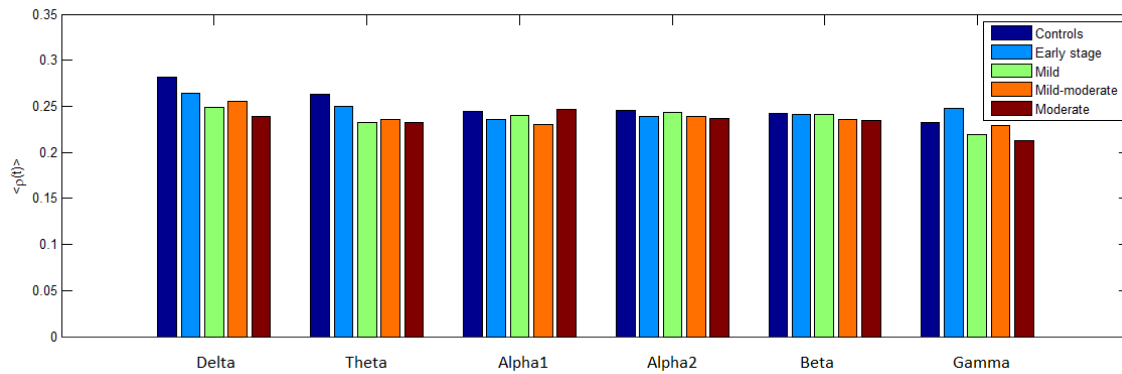


Figure 15: Average $\rho(t)$ -value for each frequency band divided into the different cohorts of the study. The average $\rho(t)$ -value does not vary much within each frequency band over the course of the disease. Only in the delta and theta frequency band a slight decrease of the average synchronisation can be seen in time.

Another way to visualize the deterministic behaviour of the dynamics is by determining the potential of $D_\rho^{(1)}(\rho, \psi)$, according to:

$$V(D^{(1)}) = - \int D^{(1)}(\rho) d\rho. \tag{24}$$

In this potential, local minima refer to stable fixed points, corresponding to the null clines of the drift coefficient (Daffertshofer, 2010). Figure 16 shows the potentials of ρ for each frequency band. Because the beta and gamma frequency band include the largest frequency range, these potentials are more profound in comparison to those of the other frequencies. Stable fixed points are seen for all frequency bands for $\rho \approx 0.2$.

The aim of this section of the study was to compare the alpha1 and beta band as is described in section 2.2. Figure 15 displays very little variability in the alpha1, alpha2, beta and gamma frequencies. In delta and theta, a slight decrease of the average $\rho(t)$ -value can be appointed. Thereby, figure 16 shows a more profound potential for the delta and theta frequency in comparison to the alpha1 and alpha2 frequencies. As a result of both figures 15 and 16, therefore, instead of alpha1 and beta, delta and theta have been chosen to be compared and analyzed in the following sections of the results.

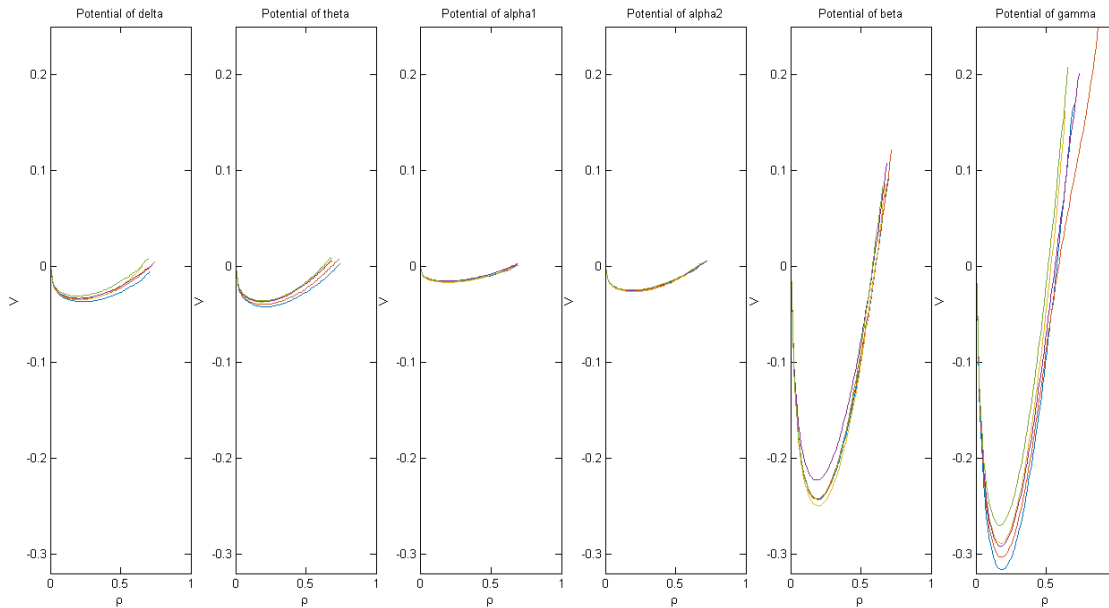


Figure 16: Potentials (V) of ρ for each frequency band. The colors indicate the cohorts of the study. Because beta and gamma have a much wider frequency range in comparison to the other frequencies, these potentials include more data points and are therefore more profound.

In the analysis of the delta and theta frequency, first, a system identification approach was applied to extract the deterministic components of the system. Thereby, $D_\rho^{(1)}(\rho, \psi)$ and $D_\psi^{(1)}(\rho, \psi)$ were estimated and analysed to qualify the system’s dynamics, similar to the analysis in section 3.1. Figure 17 displays $D_\rho^{(1)}(\rho, \psi)$ and $D_\psi^{(1)}(\rho, \psi)$ for the PD resting-state MEG data. For $D_\rho^{(1)}(\rho, \psi)$, in all cohorts, there is an average ρ -value of approximately 0.2, as indicated by the stable null cline, which is in line with figure 15 and 16. The figures for $D_\psi^{(1)}(\rho, \psi)$ represent a flat topological outline (see colour bar), indicating no structure, stability or stationarity, and ψ is therefore neutrally stable. When figure 17 is compared to the analysis of numerical simulations of the bimodal frequency distribution of the order parameters’ and oscillators’ dynamics as is displayed in figure 9C and D, it is shown that both figures display totally different topological outlines. Therefore, the bimodal frequency distribution does not seem to apply to resting-state MEG PD data to model the simultaneous changes in delta and theta frequencies³.

³ The analysis and comparison of the alpha1 and beta frequencies, as was the initial idea, was also conducted and led to the same conclusion as for analyzing and comparing the delta and theta frequencies.

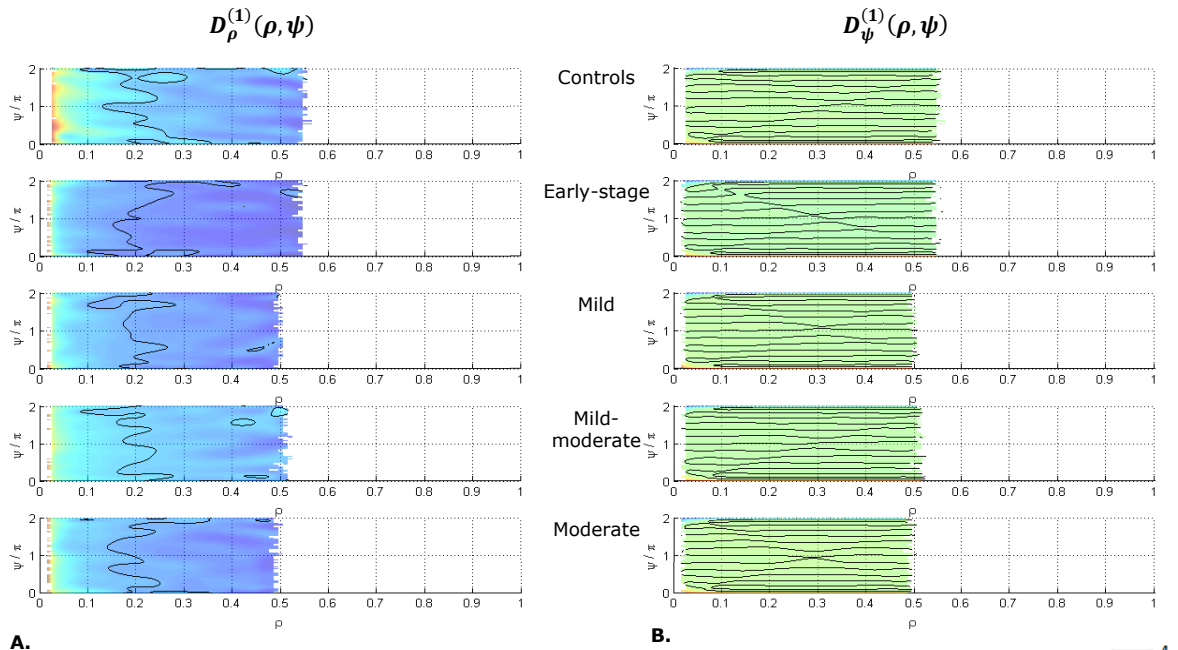


Figure 17: Two-dimensional drift coefficients $D_{\rho}^{(1)}(\rho, \psi)$ (A) and $D_{\psi}^{(1)}(\rho, \psi)$ (B) plus null clines modelled with a polynomial fit of the fifteenth order (black lines) for each cohort of the study. The null clines are stable when the contour of the figure decreases (negative slope) in height (see colorbar), or are unstable when the contour of the figure increases (positive slope) in height. C: Colour bar. The stable null cline of $D_{\rho}^{(1)}(\rho, \psi)$ does not differ much when comparing the cohorts of the study but is approximately 0.2. $D_{\psi}^{(1)}(\rho, \psi)$ shows a flat topological outline similar for all cohorts, thereby representing no structure, stability or stationarity.

4 Discussion

4.1 General conclusions

The goal of this study was to validate the applicability of a bimodal frequency distribution in the Kuramoto model to PD resting-state MEG data, whereby the study of Martens et al., including a numerical analysis of order parameters' dynamics, served as a framework (Martens et al., 2009). As an intermediate step, to resemble the finite size of the empirical data, numerical simulations of the oscillators' dynamics were created with a uni- and bimodal distribution of the natural frequencies.

The numerical simulations of the order parameters' dynamics, the similarity of the asymptotic solutions of ρ and the zero-crossings of the drift coefficient, resemble the results of the analysis of Martens and co-workers and thereby provide a proof of concept (displayed in figure 7A and C). The numerically simulated oscillators' dynamics data do not show the same behaviour in comparison to the order parameters' dynamics when the bimodal frequency distribution is applied to the Kuramoto model according to the Ott & Antonsen ansatz (Martens et al., 2009).

This study shows that PD resting-state MEG data do not exhibit similar behaviour in its bifurcation analysis in comparison to the numerical simulations of the order parameters' dynamics described by equations (15) and (16) or the numerical simulations of the oscillators' dynamics described by equation (4). The PD resting-state MEG data does not show any decrease in phase synchronization over the course of the disease and thereby $D_{\psi}^{(1)}(\rho, \psi)$ does not show any structure or value, i.e. is neutrally stable. The numerical simulations of the order parameters' and oscillators', on the other hand, show an increased state of synchronization for increasing κ - values and ψ displays structure (for this comparison, see figure 9, 13 and 17). In short, there are three possible explanations for this inequality: 1) the PD data do not display this type of behaviour; 2) the model is not applicable to this type of (empirical) data because of its finite size; 3) the behaviour of the PD data system continuous to be transient and will not reach an asymptotic solution. The following paragraphs will thoroughly describe and extend the aforementioned results and conclusions.

4.2 Previous studies

The modification of a bimodal frequency distribution in the Kuramoto model of coupled phase oscillators has been studied several times. Crawford, was the first to accurately study a nonlinear stability analysis in the case of a bimodal frequency distribution (Crawford, 1994). In 1984 however, Kuramoto wrote a book on coupled oscillators and therein started the speculation on the bifurcation analysis in a bimodally distributed population of the oscillators' natural frequencies (Kuramoto, 1984). This field of research has been extensively elaborated in the years after Kuramoto's book but is still in need for further elucidation and a wider range of applicability. As for applying the bimodal frequency distribution to experimental data, no previous research has been published.

4.3 System identification approach

In this study, the system identification approach based on the estimation of Kramers-Moyal coefficients was shown to successfully identify the deterministic components of the numerically simulated data and resting-state MEG time series of PD patients. Transient behaviour was simulated in the oscillators' dynamics, to expand the spectrum of the system. By applying perturbations to the system, its inherent features need to be preserved as described by Van Mourik and co-workers. Key for these perturbations is for them to be instantaneous and uncorrelated and the interval between perturbations needs to allow the system to recover (Van Mourik et al., 2006).

The drift coefficient was determined to analyze stable and unstable fixed points of the system, displayed in figures 8, 9, 12, 13 and 17. Especially in the two-dimensional drift coefficients of the simulated data ($D_{\rho}^{(1)}(\rho, \psi)$ and $D_{\psi}^{(1)}(\rho, \psi)$), not enough data points were recorded to create a detailed description of the behaviour of the system. A recommendation for future research therefore includes to decrease the resolution of ψ and increase its step size. The limited number of samples also holds for the PD resting-state MEG data. This limitation decreases the quality of the system identification procedure by restricting the estimation of probability densities necessary to calculate the Kramers-Moyal coefficients, and thereby the analysis of the stability of the empirical data (Van Mourik et al., 2006). A bigger sample size is therefore highly recommended in future studies, either through more trials or longer trial length. Another solution

to the limited sample size is found in statistical independence of recorded trials and stationarity of the attractor. This leads to a representative average of the individually computed probabilities to therewith compute the Kramers-Moyal coefficients (Van Mourik et al., 2006).

The second Kramers-Moyal coefficient, the diffusion coefficient, analyzes the signal dependent noise which did not cover the main interest of this study and was therefore not taken into account. However, to complete the view on the dynamics of the system, in future studies, this coefficient should be considered.

4.4 Model comparison

In the numerical simulations of the order parameters' dynamics, a polynomial function was known as described by Martens et al. (equation (13) and (14)). When this function however would not have been known and for the numerical simulations of the oscillators' dynamics, a model comparison method was applied to test for which polynomial function would best describe the data. The applicability of the AIC and BIC is thoroughly described and compared in section 2.1.1. This comparison revealed that which method to apply is dependent on multiple factors. Therefore, no choice was made between the two methods and both were applied. The results of the AIC and BIC show that both methods select the same models for each analysis and for each data set. This thereby confirms the choice for the polynomial parameters as described by Martens and co-workers.

A difficulty in determining the correct order of the polynomial function and its parameters is in the dynamics of ρ . These dynamics are described in the range from $[0,1]$, resulting in a limited range for the polynomial function to be visualized. The validity of the order of the polynomial function is questionable, although the topological outline of the system will not be affected by this.

4.5 The Ott-Antonsen ansatz

The method as set up by Martens et al., referred to as the Ott-Antonsen ansatz by the authors, forms a fundamental aspect of the current study. The ansatz holds two important assumptions: 1) an infinite amount of oscillators (thermodynamic limit); and 2) the application of a density function with low order Fourier coefficients. The simulations of the oscillators' dynamics include a finite amount of oscillators whereby finite size effects appear which thereby differs from the order parameters' dynamics. As for the second assumption, it is not known whether this is a correct approach because there seems to be a difference between the results of the order parameters' dynamics and the oscillators' dynamics. The question therefore is whether the Ott-Antonsen ansatz is the proper method to analyze the oscillators' dynamics with a bimodal frequency distribution. When more oscillators are applied in the analysis there will be less finite size effects but it is unclear how this will affect the development of the Fourier series. It might enhance the similarity of the order parameters' dynamics and the oscillators' dynamics but because of a limited computational capacity this is beyond the scope of this study.

The limits of the Ott-Antonsen ansatz are not fully clarified yet within the scope of the paper of Martens et al., including the Kuramoto model with a bimodal frequency distribution. The method is known to capture all the attractors in the case of a bimodal Kuramoto model as proposed by Martens et al., as well as for the unimodal Kuramoto model in its original form or with external periodic forcing. In other cases it does not give a complete view on the system's dynamics and this therefore needs to be elucidated. In the current study however, this dilemma did not influence the results because the method proved to be successful in the case of randomly chosen distributed frequencies of the oscillators (Martens et al., 2009).

Another assumption in the paper of Martens et al. is its symmetry between the two subpopulations. This symmetry entails $\Delta_1 = \Delta_2$, and $\omega_{0_1} = \omega_{0_2}$ (equation (8) and (9)) and results in the order parameters as described in equation (13) and (14). Because the results of the empirical data do not show symmetry between the two involved frequencies, the assumption of symmetry does not hold for this dynamical system. An extension of the analysis in the current study could be an asymmetry between the subpopulations of the frequency distribution, giving both populations different weights (Martens et al., 2009). This asymmetry will be more representative when modelling brain rhythms because as was discussed in section 4.3, the involved frequencies change in power and show a slowing of oscillations in disease progression. Thereby, the Ott-Antonsen ansatz assumes a homogenous coupling (global coupling in the Kuramoto model) although connectivity between populations will differ in comparison to connectivity within populations of oscillators. An idea for future research regarding this issue is the application of skewed distribution instead of a Lorentzian distribution to account for the differences within populations of oscillators. When the symmetry assumption is broken, the complex order parameters (equation (8) and (9)) of the system

will become uneven, resulting in a four-dimensional analysis. This system will be very complex and contains high computational effort.

The average ρ -value of approximately 0.2 for all cohorts in the empirical data indicates no decrease of overall synchronization in disease progression when analyzing the delta and theta frequency. Olde Dubbelink and co-workers found a slowing of resting-state neural oscillations which describes a shift of the involved frequencies to the left as indicated by the power spectrum. However, this shift in frequencies cannot be defined by synchronization. The amount of synchronization of a population of neurons indicates spectral power and would therefore describe the increase in low frequencies and decrease in high frequencies as was also found by Olde Dubbelink and co-workers (Olde Dubbelink et al., 2013; Stoffers et al., 2008). Because in the bimodal model for the empirical data the global order parameter was analyzed, a separate analysis of the order parameter of the delta and theta frequency was not included, and no conclusions can be drawn regarding changes in synchronization of either frequency in isolation.

In the Kuramoto model κ is the control parameter regulating the order parameter of the system, thereby influencing the state of the dynamical system. The higher κ , the more synchronized the system is, which is applicable to both the unimodal as well as the bimodal situation. The main issue in the empirical data is therefore that κ cannot be adjusted and no control parameter over the state of the system is present. To be able to simultaneously model the slowing of two or multiple frequencies in PD resting-state MEG data, phase synchronization does not seem to be the proper measure. The shift in frequencies is related to a shift in ω_0 for each separate frequency included in the bimodal model. In the method as set up by Martens and co-workers however, the included populations are symmetric, refraining the model from analyzing frequencies of unequal height (power) and not allowing the visualization of a shift in these frequencies. Therefore, again, this symmetry assumption must be questioned.

4.6 Comparison between numerical simulations and empirical data

Martens et al. describe the occurrence of standing wave states, corresponding to limit-cycle solutions, in their bifurcation analysis. They describe these standing wave states as two counter-rotating groups of oscillators, synchronized to $-\omega_0$ or $+\omega_0$. Outside of these groups the oscillators are drifting with respect to each other and to the synchronized groups. The transition from incoherence to coherence including the intermediate standing wave state, realized with increasing κ , is dependent on the degree of bimodality ($\omega_0 > \frac{\Delta}{\sqrt{3}}$) of the dynamical system (Martens et al., 2009). Figure 7C shows a shift from the dotted black line in the bimodal situation. This deflection could indicate the presence of standing wave states. A bifurcation diagram could confirm this finding when limit-cycle solutions would appear. This however is beyond the scope of this study

$D_\rho^{(1)}(\rho, \psi)$, as shown in figure 9, 13 and 17, for the order parameters' dynamics, oscillators' dynamics and empirical data respectively, show no resemblance in their topological outline. $D_\psi^{(1)}(\rho, \psi)$ shows a flat topology of the order parameters' dynamics for both the bimodal situation in figure 9 and for the empirical data in figure 17, however the values of this topology differ. Thereby, the flat topology of $D_\psi^{(1)}(\rho, \psi)$ of the empirical data does not provide any insightful information on the behaviour of the dynamical system. Overall, the conclusion that can be drawn when comparing figure 9 and 17 is that the empirical data are clearly not unimodal and adjustments to the bimodal model need to be applied to be able to analyze the empirical data.

In the numerical simulations of the oscillators' dynamics, the main point of debate comprises whether the simulations were recorded long enough. The dynamics, especially in the bimodal situation, do not seem to reach a stationary point and ρ does not exactly resemble 0 or 1 because of finite size effects⁴, caused by the finite amount of oscillators. These effects resemble erratic motion and are approached to resemble noise, referring to a stochastic process. Finite sizes, however, yield different dynamics which could lead to qualitative differences in the topological outline of the dynamical system in comparison to the order parameters' dynamics. In the generation of the order parameters' dynamics, with infinite sample size, which leads to no finite size effects, Gaussian noise was added to resemble a stochastic process. Thereby, the simulations of the order parameters' dynamics, in contrast to the simulation of the oscillators' dynamics and the empirical data, includes an infinite amount of nodes. The network and simulated duration of the oscillators' dynamics will have to be much larger to decrease the finite size effects and to conform

⁴ A set of simulated oscillator dynamics that were too short have been analyzed and described in appendix A.

to the application of the Ott-Antonsen ansatz. When after these adjustments deviations continue to be present, other phenomena are probably occurring. Then, the Ott-Antonsen ansatz might not fit to this type of data, the low-dimensional reduction method does not apply, the Kramers-Moyal expansion does not apply because the data does not show Markov properties or the method does not allow for finite sizes.

A possible resolution for the problems that arose due to the finite sample sizes of the simulations of the oscillators' dynamics and the empirical data, may come from a new analytical approach by Pikovsky and Rosenblum. In this approach, the Ott-Antonsen ansatz was placed in a more general mathematical framework which thereby captures all dynamics of the full systems, and works for any sample size. The downside of this analysis is its high complexity, and whether it actually holds for the Kuramoto model needs to be elucidated (Martens et al., 2009; Pikovsky & Rosenblum, 2008).

Another issue concerning the numerical simulations comprises its variability. A high variability would imply a better view on the behaviour of the system and better resemblance to the empirical data (which contains a high amount of noise). The oscillators' dynamics contain a high amount of variability due to the addition of many perturbations. The order parameters' dynamics by contrast, only include a small amount of noise and thereby only little variability is present.

The empirical data was initially analyzed for the alpha1 and beta frequency ranges, because these two frequencies were shown by Olde Dubbelink et al. to be changing in PD in disease progression (Olde Dubbelink et al., 2013). During the analysis however, as previously described in section 3.3, the alpha1 and beta frequency showed little variation in their average ρ -value. Because the delta and theta frequency band did show some variation, the decision was made to continue the analysis on these frequency bands. Overall however, both combinations of frequency bands displayed similar results where ψ did not show any structure or stationarity. Because of these results it should be disputed whether the bimodal distribution of the natural frequencies is a relevant method to model the simultaneous change in frequencies in PD. An implication for further research is to set up a multi modal frequency distribution. An issue of concern thereby is the complexity of this system.

5 Conclusions

A bimodal frequency distribution in phase oscillators as proposed by Martens et al. was implemented and applied to both numerically simulated and empirical data. A system identification approach was successfully applied, resembling the analytic results of the paper of Martens and co-workers. Thereby, a two-dimensional drift coefficient was extracted to model both order parameters of the dynamical system (ρ and ψ), resulting in a complex interpretation. The application of a network with a bimodal frequency distribution to resting-state MEG data of PD patients showed neutral stability for the two-dimensional drift coefficient of ψ . Thereby, the two-dimensional drift coefficient of ρ revealed a synchronization value that did not vary much as the disease progressed in time. By comparing the results of the two-dimensional drift coefficients of the numerically simulated data to the empirical data, no similarities were found in its qualitative topology. It can therefore be concluded that the bimodal frequency distribution as applied to the empirical data does not capture the simultaneous changes in oscillatory activity as previously found in PD. Also, the empirical data is clearly not unimodal. The differences between the order parameters' dynamics and the oscillators' dynamics indicate an important limitation of the Ott-Antonsen ansatz. It is therefore questionable whether this method is correct and whether it is applicable to a bimodal frequency distribution without homogeneous coupling. The main questions for further research comprise: 1) how to create a proper link between the changing frequencies related to PD?; 2) how to break the symmetry in the method as proposed by Martens et al., and is asymmetry the only adaptation or does it need tri-modality or even multi-modality?; and 3) what is the control parameter in the empirical data and how can this parameter be controlled?

Appendix A – Oscillators’ dynamics simulated too short

The first numerically simulated oscillators’ dynamics consisted of time series without asymptotic solutions and were therefore simulated too short. The parameter settings for these simulations are shown in table 6.

Table 6: Parameter settings for the numerical simulations of the oscillators’ dynamics that were simulated too short (equation (4))

Parameter	Setting
N	10 000
T	1
# nodes	500
ω_0	$(0:.1:3) * \frac{\delta_0}{\sqrt{3}}$
Δ	$\frac{(0:2)}{2}$
α	$(0:.1:3)^3$
κ	$(0:0.05:5)$
Δt	$\frac{1}{1000}$

Figure 18 displays the ‘asymptotic solution of ρ ’ which are clearly not asymptotic but show transient behavior. When comparing figure 18 to figure 7 and 11 hardly any resemblance is seen. Figure 18 shows no similarity in the behavior of the asymptotic solutions of ρ in comparison to the theoretical behavior in the unimodal situation as described by Strogatz (2000), confirming the insufficient recording time of these simulations.

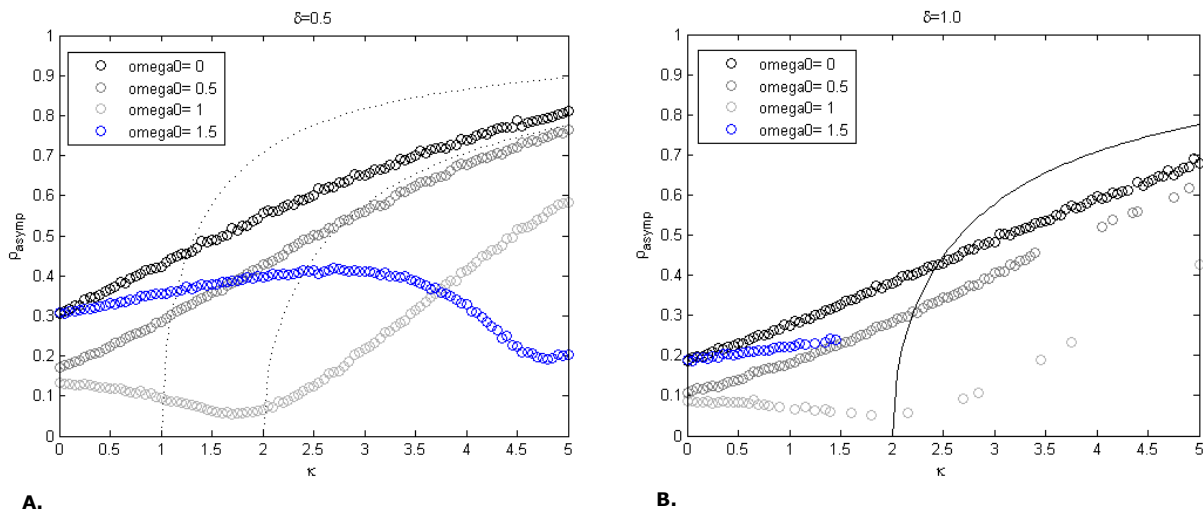


Figure 18: Numerical simulations of equation (4), the influence of the coupling strength on synchronization for two different values of Δ . The asymptotic solutions of ρ for different values of ω_0 are represented by the dots, dependent on coupling strength κ . The black dotted line represents the theoretical behaviour of ρ in the unimodal ($\kappa_c = 1$) and bimodal ($\kappa_c = 2$) situation. Both figure A and B show that no asymptotic solution and no full synchronization is reached by each time series of ρ . Thereby, for $\Delta = 1$ there are clearly not enough data points for increasing values of ω_0 .

To compare the results of these simulations to section 3.1.1 and 3.1.2, in the following sections, the times series with $\Delta = 0.5$ and $\omega_0 = 0$ and $\omega_0 = 2$ will be analyzed.

Figure 19 represents the overall behavior of $D_\rho^{(1)}(\rho, \psi)$ in the unimodal and bimodal situation, respectively. No resemblance is seen in comparing both situations to $D_\rho^{(1)}(\rho, \psi)$ of the order parameters’

dynamics. Figure 19B does show similarities to figure 11 D in the behavior of the zero-crossings of $D_\rho^{(1)}(\rho, \psi)$ after $\kappa = 3$.

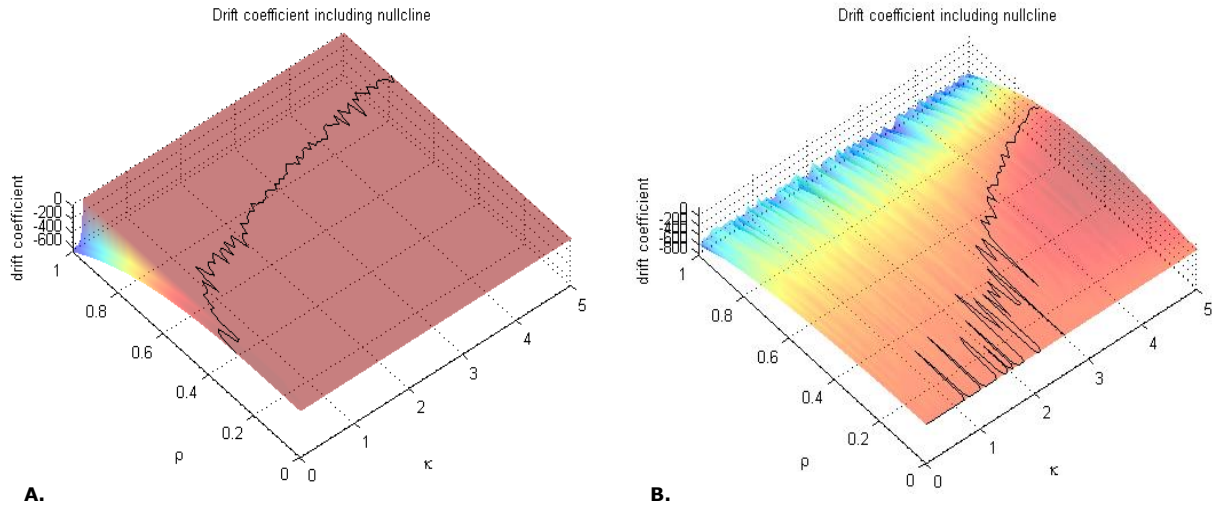


Figure 19: Numerical simulations of equation (4), total topological outline of $D_\rho^{(1)}(\rho, \psi)$ for each κ - and ρ -value including a polynomial fit of the zero crossings of $D_\rho^{(1)}(\rho, \psi)$. **A:** Unimodal situation: $\omega_0 = 0$. **B:** Bimodal situation $\omega_0 = 2$. For both situations, very low values of $D_\rho^{(1)}(\rho, \psi)$ are shown and no similarities are seen when comparing $D_\rho^{(1)}(\rho, \psi)$ to the order parameters' dynamics although when compared to the oscillators' dynamics, a similarity is seen in the behavior of the zero-crossings of $D_\rho^{(1)}(\rho, \psi)$ after $\kappa = 3$.

Figure 20 shows results of $D_\rho^{(1)}(\rho, \psi)$ for three different κ -values. When comparing the unimodal to the bimodal situation, it is shown that the topological outline of both systems do not differ qualitatively. As described previously for the oscillators' dynamics in section 3.1.2, the polynomial function which is derived from the paper of Martens and co-workers, is not a proper fit as is also visualized in figure 20.

When comparing figure 20 to figure 12 it is visualized that topological outline of both systems do not differ qualitatively, except for figure 20A where a stable fixed point is shown which is not present in figure 12A.

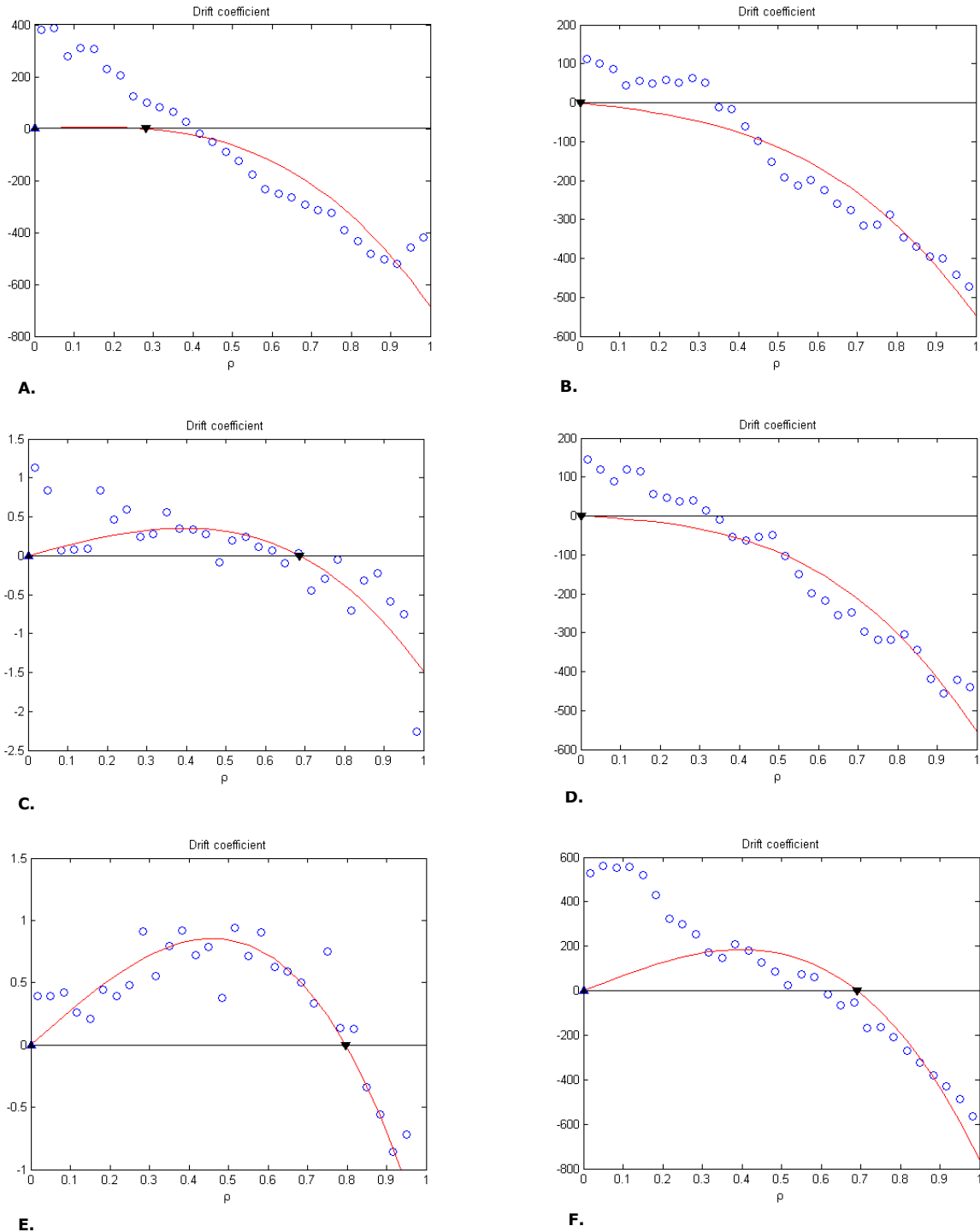


Figure 20: $D_{\rho}^{(1)}(\rho, \psi)$ (blue dots) with a polynomial fit (red line), including unstable fixed points (triangle pointing upwards) and stable fixed points (triangle pointing downwards). The stable fixed points are appointed by the zero crossings of the polynomial fit where the derivative of $D_{\rho}^{(1)}(\rho, \psi)$ is negative. The unstable fixed points are appointed by the zero crossings of the polynomial fit where the derivative of $D_{\rho}^{(1)}(\rho, \psi)$ is positive. **A:** Unimodal situation: $\omega_0 = 0, \kappa = 0$. **B:** Bimodal situation: $\omega_0 = 2, \kappa = 0$. **A:** As $\kappa < \kappa_c$ an unexpected stable fixed point appears for $\rho \approx 0.3$, indicating partial synchronization of the system. **B:** As $\kappa < \kappa_c$ an unstable fixed point appears for a very low value of ρ , representing asynchrony in the dynamical system. **C:** Unimodal situation: $\omega_0 = 0, \kappa = 2.5$. As $\kappa > \kappa_c$, a stable fixed point appears, showing partial synchronization of the dynamical system. **D:** Bimodal situation: $\omega_0 = 2, \kappa = 2.5$. As $\kappa < \kappa_c$ an unstable fixed point appears for a very low value of ρ , representing asynchrony in the dynamical system. **E:** Unimodal situation: $\omega_0 = 0, \kappa = 5$. **F:** Bimodal situation: $\omega_0 = 2, \kappa = 5$. **E & F:** As $\kappa > \kappa_c$, a stable fixed point appears, showing partial synchronization of the dynamical system.

$D_\rho^{(1)}(\rho, \psi)$ and $D_\psi^{(1)}(\rho, \psi)$ are visualized in figure 21 in the unimodal and bimodal situation. Figure 21B displays that ψ shows no nullclines which deviates from the values of ψ of the order parameters' dynamics and oscillators' dynamics. Thereby, these values are unexpected because in the unimodal situation there is only one population so no phase difference should be present. In the bimodal situation $D_\psi^{(1)}(\rho, \psi)$ does show values, which is similar to $D_\psi^{(1)}(\rho, \psi)$ of the order parameters' dynamics. The topological outline of $D_\rho^{(1)}(\rho, \psi)$ does resemble that of the order parameters' and oscillators' dynamics (as displayed in figure 9 and 13) qualitatively. This is also confirmed by combining both figures for $D_\rho^{(1)}(\rho, \psi)$ and $D_\psi^{(1)}(\rho, \psi)$, whereby fixed points of the system can be localized as is previously described in section 3.1.1.

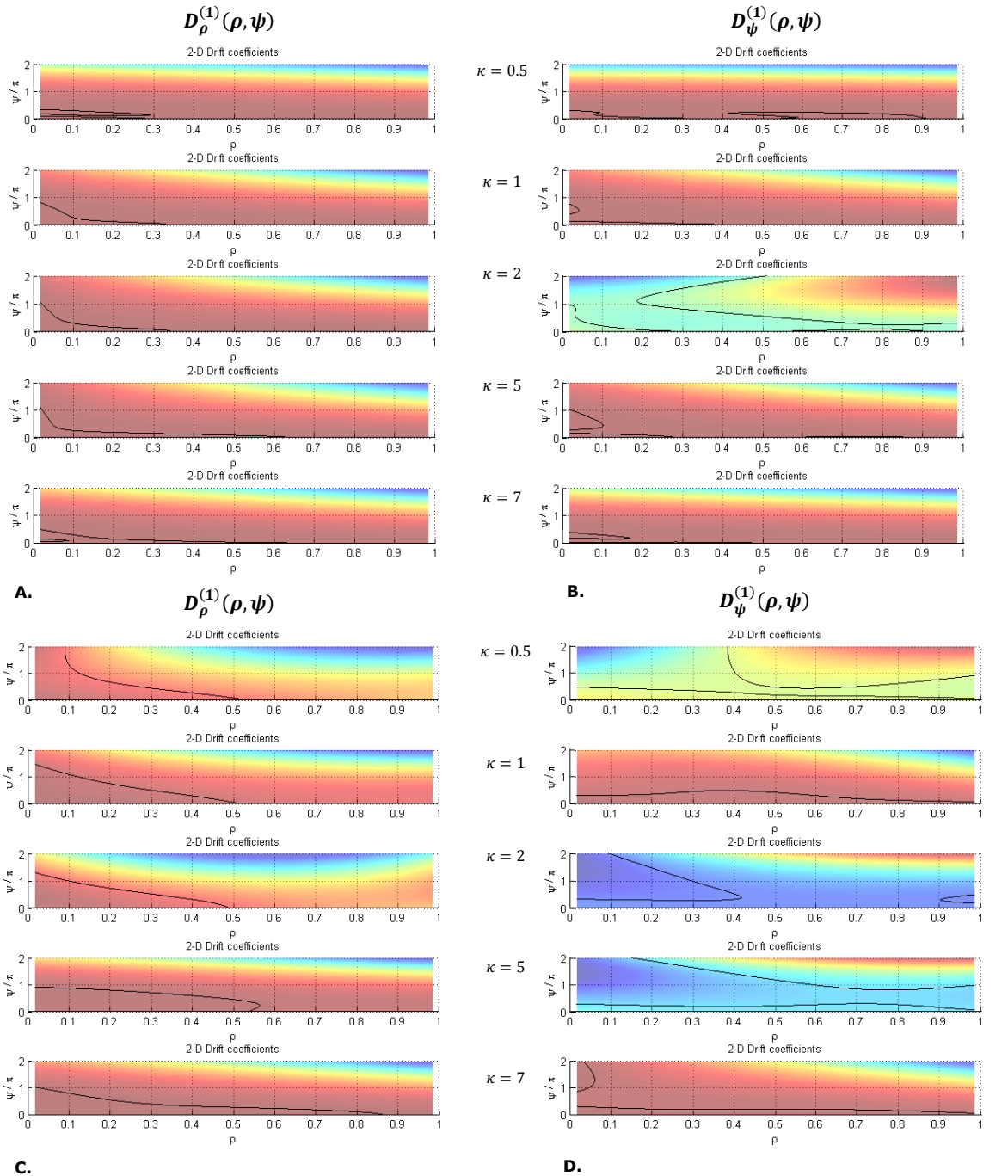
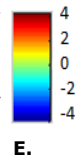


Figure 21: Two-dimensional drift coefficients $D_{\rho}^{(1)}(\rho, \psi)$ (**A** and **C**) and $D_{\psi}^{(1)}(\rho, \psi)$ (**B** and **D**) plus null clines (black lines) for different κ -values. The null clines are stable when the contour of the figure decreases (negative slope) in height (see colorbar), or are unstable when the contour of the figure increases (positive slope) in height. **A and B:** Unimodal situation ($\omega_0 = 0$). **C and D:** Bimodal situation ($\omega_0 = 2$). **E:** Colour bar indicating the height of the contour colors. When comparing $D_{\rho}^{(1)}(\rho, \psi)$ in the uni- and bimodal situation no big differences can be seen in the topological outline of the system, although in the bimodal situation the system starts to synchronize for a higher value of κ . For $D_{\psi}^{(1)}(\rho, \psi)$, the figure displays no stable null clines in the unimodal situation.



Appendix B – Model comparison

The AIC and BIC values for each κ -value, as applied to the order parameters’ dynamics, are displayed in figure 22. This figure shows that for each value of κ and in both the uni- and bimodal situation, model 2 ($f_2(\rho) = a\rho + b\rho^3$) has the lowest AIC and BIC values. The parameters of the polynomial function as described by Martens and co-workers are thereby confirmed.

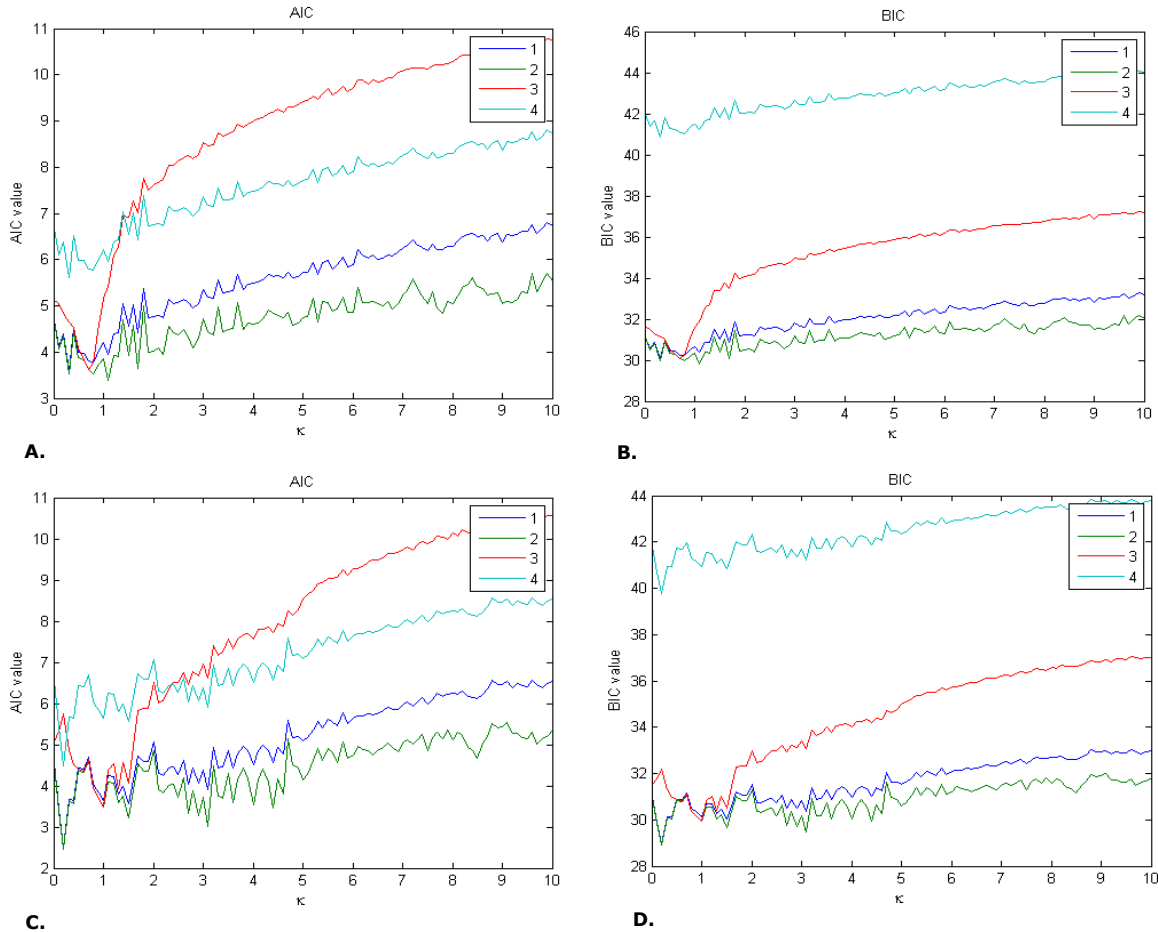


Figure 22: AIC and BIC values for each κ -value for the order parameters’ times series. The colored lines indicate each model that was compared in this analysis. An overview of the included models is given in table 2 (section 2.1.1). **A & B:** AIC (**A**) and BIC (**B**) values in the unimodal situation: $\omega_0 = 0$. **C & D:** AIC and BIC values in the bimodal situation: $\omega_0 = 2$. These figures show that for each situation and for both the AIC and BIC, model 2 ($f_2(\rho) = a\rho + b\rho^3$) contains the lowest values and is appointed as the best model to fit the order parameters’ times series.

The AIC and BIC values for each κ -value, as applied to the oscillators’ dynamics, are displayed in figure 22. This figure shows that for each value of κ and in both the uni- and bimodal situation, model 2 ($f_2(\rho) = a\rho + b\rho^3$) has the lowest AIC and BIC values. The parameters of the polynomial function as described by Martens and co-workers are thereby again confirmed.

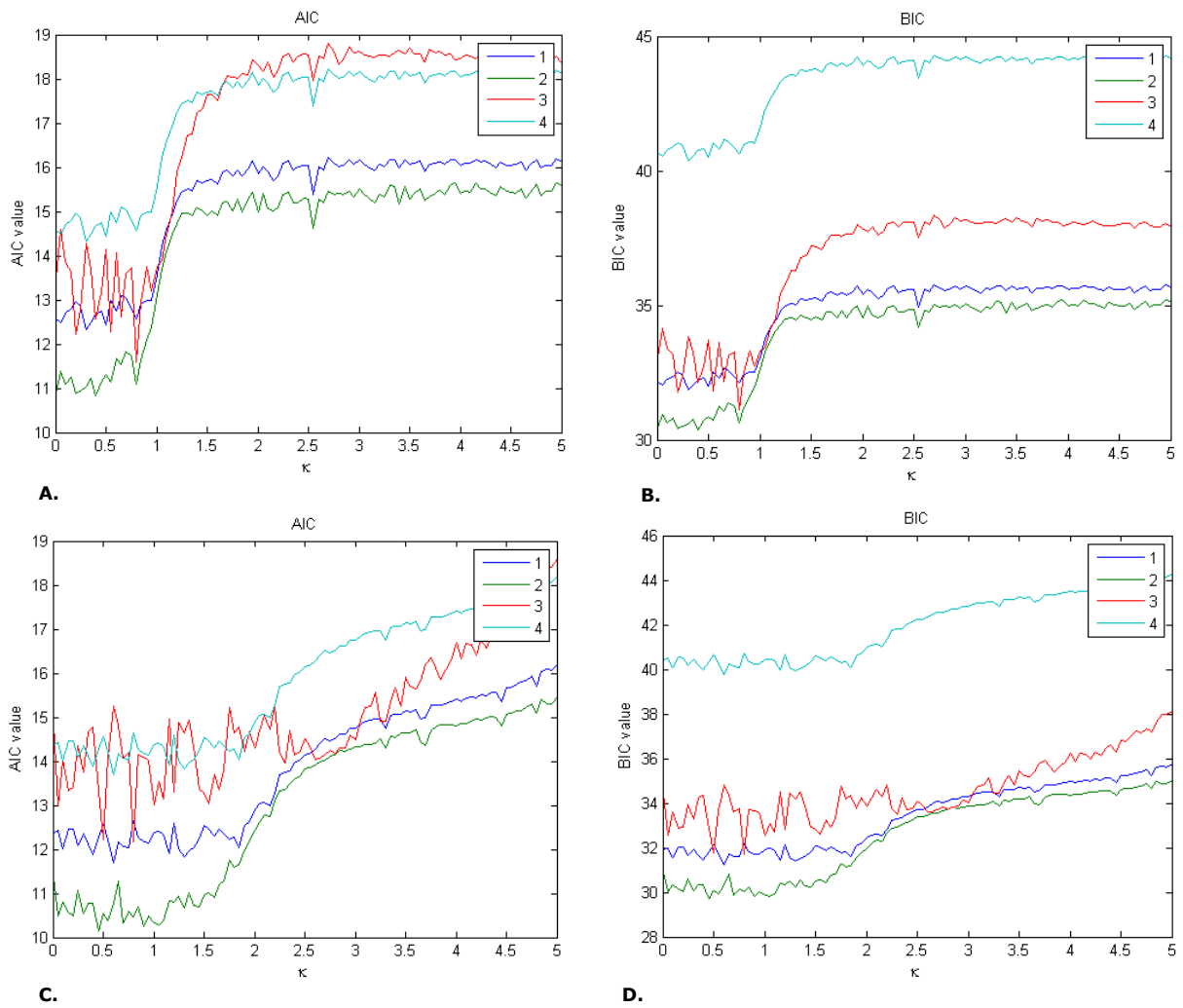


Figure 23: AIC and BIC values for each κ -value for the order parameters' times series. The colored lines indicate each model that was compared in this analysis. An overview of the included models is given in table 2 (section 2.1.1). **A & B:** AIC (**A**) and BIC (**B**) values in the unimodal situation: $\omega_0 = 0$. **C & D:** AIC and BIC values in the bimodal situation: $\omega_0 = 2$. These figures show that for each situation and for both the AIC and BIC, model 2 ($f_2(p) = ap + bp^3$) contains the lowest values and is appointed as the best model to fit the order parameters' times series.

6 References

- Acebrón, J. A., Bonilla, L. L., Vicente, C. J. P., Ritort, F., & Spigler, R. (2005). The Kuramoto model: A simple paradigm for synchronization phenomena. *Reviews of Modern Physics*, 77(1), 137–185. <http://doi.org/10.1103/RevModPhys.77.137>
- Aho, K., Derryberry, D., & Peterson, T. (2014). Model selection for ecologists: The worldviews of AIC and BIC. *Ecology*, 95(3), 631–636. <http://doi.org/10.1890/13-1452.1>
- Berendse, H. W., & Stam, C. J. (2007). Stage-dependent patterns of disturbed neural synchrony in Parkinson's disease. *Parkinsonism and Related Disorders*, 13(SUPPL. 3), 440–445. [http://doi.org/10.1016/S1353-8020\(08\)70046-4](http://doi.org/10.1016/S1353-8020(08)70046-4)
- Breakspear, M., Heitmann, S., & Daffertshofer, A. (2010). Generative models of cortical oscillations: neurobiological implications of the kuramoto model. *Frontiers in Human Neuroscience*, 4(November), 190. <http://doi.org/10.3389/fnhum.2010.00190>
- Burnham, K. P., Anderson, D. R. (2004). Multimodel Inference: Understanding AIC and BIC in Model Selection. *Sociological Methods & Research*, 33(2), 261–304. <http://doi.org/10.1177/0049124104268644>
- Buzsáki, G. (2006). *Rhythms of the brain*. New York, New York: Oxford University Press Inc. <http://doi.org/10.1093/acprof:oso/9780195301069.001.0001>
- Coopmans, F. M. T. (2013). Hubness and synchronisation of scale-free coupled phase oscillators and the relation to neurodegenerative diseases Qualification : MSc in Human Movement Sciences, (October).
- Crawford, J. D. (1994). Amplitude expansions for instabilities in populations of globally-coupled oscillators. *Journal of Statistical Physics*, 74(5-6), 1047–1084. <http://doi.org/10.1007/BF02188217>
- Daffertshofer, A. (2010). Benefits and pitfalls in analyzing noise in dynamical systems - On stochastic differential equations and system identification. *Studies in Computational Intelligence*, 328, 35–68. http://doi.org/10.1007/978-3-642-16262-6_2
- Deco, G., Buehlmann, A., Masquelier, T., & Hugues, E. (2011). The role of rhythmic neural synchronization in rest and task conditions. *Frontiers in Human Neuroscience*, 5(February), 4. <http://doi.org/10.3389/fnhum.2011.00004>
- Engel, A. K., & Fries, P. (2010). Beta-band oscillations-signalling the status quo? *Current Opinion in Neurobiology*, 20(2), 156–165. <http://doi.org/10.1016/j.conb.2010.02.015>
- Fell, J., & Axmacher, N. (2011). The role of phase synchronization in memory processes. *Nature Reviews Neuroscience*, 12(2), 105–118. <http://doi.org/10.1038/nrn2979>
- Ferreira, L. K., & Busatto, G. F. (2013). Resting-state functional connectivity in normal brain aging. *Neuroscience and Biobehavioral Reviews*, 37(3), 384–400. <http://doi.org/10.1016/j.neubiorev.2013.01.017>
- Kuramoto, Y. (1984). *Chemical Oscillators, Waves and Turbulence*. Berlin: Springer.
- Martens, E. a., Barreto, E., Strogatz, S. H., Ott, E., So, P., & Antonsen, T. M. (2009). Exact results for the Kuramoto model with a bimodal frequency distribution. *Physical Review E - Statistical, Nonlinear, and Soft Matter Physics*, 79(2), 1–11. <http://doi.org/10.1103/PhysRevE.79.026204>
- Olde Dubbelink, K. (2014). Brain network dynamics in Parkinson's disease: understanding and predicting cognitive decline (pp. 9–16). Amsterdam.
- Olde Dubbelink, K. T. E., Stoffers, D., Deijen, J. B., Twisk, J. W. R., Stam, C. J., & Berendse, H. W. (2013). Cognitive decline in Parkinson's disease is associated with slowing of resting-state brain activity: A longitudinal study. *Neurobiology of Aging*, 34(2), 408–418. <http://doi.org/10.1016/j.neurobiolaging.2012.02.029>
- Olde Dubbelink, K. T. E., Stoffers, D., Deijen, J. B., Twisk, J. W. R., Stam, C. J., Hillebrand, A., & Berendse, H. W. (2013). Resting-state functional connectivity as a marker of disease progression in Parkinson's disease: A longitudinal MEG study. *NeuroImage: Clinical*, 2, 612–619. <http://doi.org/10.1016/j.nicl.2013.04.003>
- Ott, E., & Antonsen, T. M. (2008). Low Dimensional Behavior of Large Systems of Globally Coupled Oscillators,

1–16. <http://doi.org/10.1063/1.2930766>

- Pikovsky, A., & Rosenblum, M. (2008). Partially integrable dynamics of hierarchical populations of coupled oscillators. *Physical Review Letters*, *101*(December), 1–4. <http://doi.org/10.1103/PhysRevLett.101.264103>
- Rubchinsky, L L, Park, C, Worth, R. M. (2013). Intermittent neural synchronization in Parkinson ' s disease, *68*(3), 329–346. <http://doi.org/10.1007/s11071-011-0223-z>. Intermittent
- Sadaghiani, S., HesseImann, G., Friston, K. J., & Kleinschmidt, A. (2010). The relation of ongoing brain activity, evoked neural responses, and cognition. *Frontiers in Systems Neuroscience*, *4*(June), 20. <http://doi.org/10.3389/fnsys.2010.00020>
- Schnitzler, A., & Gross, J. (2005). Normal and pathological oscillatory communication in the brain. *Nature Reviews. Neuroscience*, *6*(4), 285–296. <http://doi.org/10.1038/nrn1650>
- Sejnowski, T. J., & Poggio, T. a. (2007). *Dynamical Systems in Neuroscience Computational Neuroscience. Dynamical Systems* (Vol. 25). <http://doi.org/10.1017/S0143385704000173>
- Stoffers, D., Bosboom, J. L. W., Deijen, J. B., Wolters, E. C., Stam, C. J., & Berendse, H. W. (2008). Increased cortico-cortical functional connectivity in early-stage Parkinson's disease: An MEG study. *NeuroImage*, *41*(2), 212–222. <http://doi.org/10.1016/j.neuroimage.2008.02.027>
- Strogatz, S. H. (2000). From Kuramoto to Crawford: exploring the onset of synchronization in populations of coupled oscillators. *Physica D: Nonlinear Phenomena*, *143*(1-4), 1–20. [http://doi.org/10.1016/S0167-2789\(00\)00094-4](http://doi.org/10.1016/S0167-2789(00)00094-4)
- Van Mourik, a. M., Daffertshofer, a., & Beek, P. J. (2006). Estimating Kramers-Moyal coefficients in short and non-stationary data sets. *Physics Letters, Section A: General, Atomic and Solid State Physics*, *351*(1-2), 13–17. <http://doi.org/10.1016/j.physleta.2005.10.066>
- Van Mourik, A. M., Daffertshofer, A., & Beek, P. J. (2006). Deterministic and stochastic features of rhythmic human movement. *Biological Cybernetics*, *94*(3), 233–244. <http://doi.org/10.1007/s00422-005-0041-9>
- van Wijk, B. C. M., Beek, P. J., & Daffertshofer, A. (2012). Neural synchrony within the motor system: what have we learned so far? *Frontiers in Human Neuroscience*, *6*(September), 1–15. <http://doi.org/10.3389/fnhum.2012.00252>
- Ward, E. J. (2008). A review and comparison of four commonly used Bayesian and maximum likelihood model selection tools. *Ecological Modelling*, *211*(1-2), 1–10. <http://doi.org/10.1016/j.ecolmodel.2007.10.030>